Atmos. Chem. Phys., 18, 13813–13838, 2018
https://doi.org/10.5194/acp-18-13813-2018

Atmospheric Chemistry and Physics
Open Access
EGU

Modeling the formation and composition of secondary organic aerosol from diesel exhaust using parameterized and semi-explicit chemistry and thermodynamic models

Sailaja Eluri[1], Christopher D. Cappa[2], Beth Friedman[3], Delphine K. Farmer[3], and Shantanu H. Jathar[1]

[1]Department of Mechanical Engineering, Colorado State University, Fort Collins, CO, 80523, USA
[2]Department of Civil and Environmental Engineering, University of California Davis, Davis, CA, 95616, USA
[3]Department of Chemistry, Colorado State University, Fort Collins, CO, 80523, USA

Correspondence: Shantanu H. Jathar (shantanu.jathar@colostate.edu)

Received: 14 November 2017 – Discussion started: 13 December 2017
Revised: 21 June 2018 – Accepted: 22 June 2018 – Published: 1 October 2018

Abstract. Laboratory-based studies have shown that combustion sources emit volatile organic compounds that can be photooxidized in the atmosphere to form secondary organic aerosol (SOA). In some cases, this SOA can exceed direct emissions of primary organic aerosol (POA). Jathar et al. (2017a) recently reported on experiments that used an oxidation flow reactor (OFR) to measure the photochemical production of SOA from a diesel engine operated at two different engine loads (idle, load), two fuel types (diesel, biodiesel), and two aftertreatment configurations (with and without an oxidation catalyst and particle filter). In this work, we used two different SOA models, the Volatility Basis Set (VBS) model and the Statistical Oxidation Model (SOM), to simulate the formation and composition of SOA for those experiments. Leveraging recent laboratory-based parameterizations, both frameworks accounted for a semi-volatile and reactive POA; SOA production from semi-volatile, intermediate-volatility, and volatile organic compounds (SVOC, IVOC and VOC); NO_x-dependent parameterizations; multigenerational gas-phase chemistry; and kinetic gas–particle partitioning. Both frameworks demonstrated that for model predictions of SOA mass to agree with measurements across all engine load–fuel–aftertreatment combinations, it was necessary to model the kinetically limited gas–particle partitioning in OFRs and account for SOA formation from IVOCs, which were on average found to account for 70 % of the model-predicted SOA. Accounting for IVOCs, however, resulted in an average underprediction of 28 % for OA atomic O : C ratios. Model predictions of the gas-phase organic compounds (resolved in carbon and oxygen space) from the SOM compared favorably to gas-phase measurements from a chemical ionization mass spectrometer (CIMS), substantiating the semi-explicit chemistry captured by the SOM. Model–measurement comparisons were improved on using SOA parameterizations corrected for vapor wall loss. As OFRs are increasingly used to study SOA formation and evolution in laboratory and field environments, models such as those developed in this work can be used to interpret the OFR data.

1 Introduction

Combustion-related aerosols are an important contributor to urban and global air pollution and have impacts on climate (Pachauri et al., 2014) and human health (Anderson et al., 2012). While direct particle emissions from combustion sources are dominated by primary organic aerosol (POA) and black carbon (Bond et al., 2004), these sources also emit volatile organic compounds (VOCs) that can photochemically react in the atmosphere to form secondary organic aerosol (SOA) (Robinson et al., 2007). SOA production from combustion emissions is poorly understood and not very well represented in models in terms of its precursors, gas–particle partitioning, composition, and properties (Fuzzi et al., 2015). Atmospheric models frequently underpredict SOA mass concentrations during strong photochemical episodes in urban areas (Jathar et al., 2017b), which likely highlights the challenge in modeling the SOA contributions

from urban, combustion-related emissions (Ensberg et al., 2014).

Diesel-powered sources, which are an important source of air pollution at urban and regional scales, emit precursors that form SOA in the atmosphere (Gentner et al., 2017). Robinson et al. (2007) found that photochemical processing of exhaust emissions from a small off-road diesel engine led to SOA production and doubled the primary aerosol mass over a few hours in an environmental chamber. Chirico et al. (2010) and Gordon et al. (2014) performed similar chamber experiments on tailpipe emissions from in-fleet, on-road diesel vehicles run on chassis dynamometers. Both found SOA production that was roughly consistent with the findings from Robinson et al. (2007). They additionally found that the use of aftertreatment devices (diesel oxidation catalysts and diesel particulate filters) substantially reduced SOA production (mimicking the reduction in primary aerosol emissions) but observed some SOA production during cold starts and/or regeneration events when the proper functioning of the aftertreatment devices was limited. Furthermore, Gordon et al. (2014) found negligible differences in the SOA formation between diesel and biodiesel fuel. To access longer equivalent photochemical aging timescales compared to typical chamber experiments, Tkacik et al. (2014) measured SOA formation using an oxidation flow reactor (OFR) from air sampled from a highway tunnel in Pittsburgh, PA, used by both on-road gasoline and diesel vehicles. OFRs use high concentrations of atmospheric oxidants, e.g., hydroxyl radicals, to achieve long exposures on short actual timescales; further discussion is provided below. Tkacik et al. (2014) measured much stronger SOA formation compared to chambers (SOA : POA was 10 : 1) over photochemical exposures equivalent to 2 to 3 days, but found that the SOA was lost, or destroyed, as the mixture continued to age over the timescale of a week. Recently, Jathar et al. (2017a) performed experiments using an OFR to measure the photochemical production of SOA from an off-road diesel engine operated at various engine load, fuel, and aftertreatment configurations. Jathar et al. (2017a) found that efficient combustion at higher engine loads and removal of SOA precursors by aftertreatment systems reduced SOA production by factors of 2 to 10. The only exception was that the aftertreatment system did not seem to reduce SOA production at idle loads possibly because the exhaust temperatures were low enough to limit removal of SOA precursors in the oxidation catalyst. Overall, these studies indicate that diesel exhaust contributes to atmospheric SOA production, although the precise production of SOA varies across dimensions of photochemical age, engine duty cycle, use of alternative fuels, and aftertreatment devices.

OFRs are being used to study the photochemical production of SOA from both anthropogenic (e.g., Ortega et al., 2016) and natural (e.g., Palm et al., 2016) sources. Most OFRs used for SOA studies are 10 to 15 L flow-through metal reactors with lamps that can produce high concentrations of atmospheric oxidants to simulate photochemical processing (e.g., Lambe et al., 2011). Flows through an OFR allow for residence times between 1 and 4 min, but given the high oxidant concentrations OFRs can simulate several weeks of photochemistry. OFRs have three distinct advantages over environmental chambers. First, OFRs are smaller in size and easier to operate than environmental chambers, which allows for shorter experiments and makes them ideal for field deployments (Palm et al., 2016; Simonen et al., 2017). Second, production of high oxidant concentrations in OFRs allows for much longer photochemical exposures ($\sim$ factor of 10) than those possible with chambers (Lambe et al., 2011). Third, due to their flow-through nature, OFRs have shorter residence times than conventional chambers ($\sim$ 1–4 min) and hence are less susceptible to gas and particle losses that can influence SOA formation (Zhang et al., 2014; Krechmer et al., 2016). Despite those advantages, there are concerns that the accelerated chemistry and limitations to gas–particle partitioning may affect the formation and composition of SOA in OFRs, which calls into question their relevance in understanding SOA formation in the real atmosphere (Palm et al., 2016; Jathar et al., 2017a; Ahlberg et al., 2017). For example, short residence times and/or small condensation sinks from preexisting aerosol may not allow for complete condensation of SOA vapors (Lambe et al., 2015). Similarly, high oxidant concentrations in OFRs may lead to molecules undergoing a greater number of reactions in the gas phase before condensing, including reactions that lead to fragmentation and formation of higher volatility products (Kroll et al., 2009). Both effects will typically suppress SOA production. With the increased use of OFRs, there is a need to develop and use modeling tools that can account for fragmentation reactions and kinetic gas–particle partitioning. This will allow for a more accurate interpretation of OFR data and facilitate translation of OFR results to the real atmosphere.

Models used to simulate the photochemical production of SOA from VOCs in combustion emissions have traditionally used the two-product (Odum et al., 1996) or the more generalized n-product Volatility Basis Set (VBS) framework (Donahue et al., 2006a). In this framework, VOC oxidation products are lumped into volatility bins based on their effective saturation concentrations (C^*) and where the saturation concentration determines the partitioning of the products between the gas and particle phases (Pankow, 1994). This framework has been widely used in both box (Dzepina et al., 2009; Hodzic et al., 2010; Jathar et al., 2014a; Hayes et al., 2015) and three-dimensional (Murphy and Pandis, 2009; Tsimpidi et al., 2009; Jathar et al., 2011; Ahmadov et al., 2012; Konovalov et al., 2015) models to simulate the chemistry and gas–particle partitioning of SOA. While this framework offers a simple and computationally efficient scheme to model SOA formation, the use of volatility alone neither tracks the molecular composition nor informs the continued multigenerational chemistry that will determine the atmospheric evolution and properties of SOA. As a result,

volatility-based models have been challenged in leveraging observations of the elemental composition of SOA (e.g., atomic O : C ratios) that have become possible through the use of the aerosol mass spectrometer (AMS) to constrain parameterizations or test model predictions. Further, most volatility-based models have employed ad hoc parameterizations to model multigenerational chemistry that do not account for fragmentation reactions (Robinson et al., 2007) and possibly double count SOA formation (Jathar et al., 2016). Therefore, there is a demand to develop models that can provide an improved representation of the chemistry that governs the formation, composition, and properties of SOA.

Previously, volatility-based SOA models have been used to predict photochemical production of SOA from motor vehicle exhaust (Robinson et al., 2007; Jathar et al., 2014b; Tkacik et al., 2014). These modeling studies have shown that speciated SOA precursors such as long alkanes (C_{6-12}) and single-ring aromatics (e.g., benzene, toluene) explain less than 20 % of the observed SOA and have argued that the remainder of the SOA (~ 80 %) arises from the photooxidation of typically unspeciated organic compounds. These unspeciated compounds, also referred to as intermediate volatility organic compounds (IVOCs), are likely species with carbon numbers larger than 12 and appear as an unresolved complex mixture on using traditional gas chromatography–mass spectrometry (GC-MS) techniques (Presto et al., 2011). Early estimates of IVOC emissions and their SOA potential have significantly improved predictions of the SOA formed from diesel exhaust (Jathar et al., 2014b) and have broadly improved OA model performance in three-dimensional large-scale models (Murphy and Pandis, 2009; Pye and Seinfeld, 2010; Jathar et al., 2011; Tsimpidi et al., 2009). Consider as an example that Zhao et al. (2015), using a thermal desorption GC-MS to provide detailed speciation of the carbon-number resolved linear, branched, and cyclic alkane IVOCs in diesel exhaust, found that these species accounted for up to 60 % of the non-methane organic gas emissions. While IVOCs have been recognized as an important class of SOA precursors for diesel (and even for gasoline and biomass burning) sources, updated emissions and speciation estimates from Zhao et al. (2015) have not yet been used to explain observations of photochemically produced SOA from diesel exhaust.

Recently, several model frameworks have been developed to improve the representation of SOA formation, considering dimensions of SOA beyond just volatility. The Statistical Oxidation Model (SOM) developed by Cappa and Wilson (2012) is one such example, although volatility remains an important consideration. The SOM is a semi-explicit, parameterizable mechanism that uses a two-dimensional carbon–oxygen grid to simulate the multigenerational chemistry and gas–particle partitioning of organic compounds. Although the SOM does not explicitly track or specify the product species composition (e.g., functional groups), the carbon- and oxygen-number representation provides adequate detail to represent many key atmospheric processes, e.g., reactions with oxidants, formation of functionalized products, scission of carbon backbones or fragmentation, and surface and condensed-phase chemistry and gas–particle partitioning. The SOM has been used to interpret chamber experiments (Zhang et al., 2014; Cappa et al., 2013; Cappa and Wilson, 2012) and was recently integrated into a chemical transport model (Jathar et al., 2015) to examine the influence of multigenerational aging (Jathar et al., 2016) and chamber-based vapor wall losses (Cappa et al., 2016) on ambient concentrations and properties of OA. The two-dimensional VBS (2D-VBS) (Donahue et al., 2011) and the carbon–polarity grid of Pankow and Barsanti (2009) are examples of similar frameworks. These more sophisticated models (i.e., SOM, 2D-VBS, carbon–polarity grid) have not yet been employed to study SOA formation from complex mixtures such as combustion emissions.

To summarize, combustion sources such as diesel-powered sources emit precursors that can photooxidize in the atmosphere to produce SOA. This SOA production is dependent not only on the precursor composition (that could vary by combustion mode and fuel type) and photochemical age, but also on the experimental artifacts (e.g., short condensation timescales) introduced by OFRs. Hence, there is a need to develop and apply sophisticated, yet computationally efficient, numerical models to simulate and study SOA formation from combustion emissions. In this work, we applied two SOA model frameworks that vary in sophistication (VBS and SOM) to simulate the photochemical production of SOA in an OFR from diesel exhaust. The models were evaluated by comparing model predictions (OA and O : C) to the recent measurements made by Jathar et al. (2017a), where SOA production was quantified for different photochemical ages under varying engine loads, fuels, and aftertreatment devices. The model–measurement comparison, along with sensitivity simulations, highlights the importance of modeling the kinetic gas–particle partitioning of SOA in OFRs, the contribution of IVOCs to the total SOA production, and the ability of the SOM to accurately track the composition of SOA.

2 Methods

2.1 Experiments and data

Jathar et al. (2017a) performed photooxidation experiments using an OFR to measure SOA production from the exhaust of a 4.5 L John Deere diesel engine. The stock engine met Tier 3 emissions standards for off-road diesel engines. The OFR used therein was described in detail by Friedman et al. (2016) and the experimental setup and OA measurements from these experiments were described in detail by Jathar et al. (2017a). We briefly summarize the experimental setup, measurements, and findings from Jathar et al. (2017a). The engine was run at two different loads (idle and 50 % load)

with two different fuels (diesel and biodiesel) and with and without an aftertreatment system. The aftertreatment system included a diesel oxidation catalyst (DOC) to oxidize CO and total hydrocarbons (THC) and a diesel particle filter (DPF) to trap fine particles. Diesel exhaust was diluted by a factor of 45–110 before entering the OFR. The intensity of the mercury lamps (at wavelengths of 185 and 254 nm) inside the OFR was varied to produce different hydroxyl radical (OH) concentrations and simulate different photochemical exposures. The OFR had a residence time of 100 s. A suite of instrumentation was used to measure gas-phase (CO_2, CO, THC, NO_x, O_2, oxygenated organic compounds) and particle-phase (aerosol size and composition) concentrations. A total of 13 experiments (see Table 1 for more details) were performed at varying engine loads and with varying fuels and aftertreatment configurations. The OH exposure was varied between 0 and a maximum of 9.2×10^7 molecules-h cm^{-3} (equivalent to 2 days of photochemical aging at an OH concentration of 1.5×10^6 molecules cm^{-3}). On average, each experiment included measurements at six to seven different photochemical exposures. The mass concentrations and elemental composition of the POA (measured when OFR lights were off) and SOA (at varying OH exposures) were measured by a high-resolution aerosol mass spectrometer (HR-AMS). In addition to the measurements reported by Jathar et al. (2017a), the gas-phase concentrations of oxygenated organic compounds were measured by an acetate reagent ion-based chemical ionization mass spectrometer (CIMS) (Link et al., 2016). At all engine configurations, SOA production exceeded the POA emissions after the equivalent of a few hours of atmospheric photochemical aging. SOA production was particularly strong at idle (or less fuel-efficient) engine loads and/or when exhaust temperatures were low and proper functioning of the aftertreatment devices was limited. Further, POA emissions and SOA production were nearly identical between diesel and biodiesel fuels. A synopsis of experiments performed and the THC, which includes all SOA precursors CO, NO_x, POA, SOA, O : C, OH, and size distribution, is presented in Table 1.

Although the diesel exhaust was diluted with clean air to produce atmospherically relevant concentrations of POA, the initial THC, CO, and NO_x concentrations in the OFR were still quite high. Peng and Jimenez (2017), using a detailed gas-phase model, argued that the high external OH reactivity from high THC, CO, and NO_x concentrations might lead to non-OH chemistry in the OFR and NO could quickly be consumed in the OFR leading to low NO conditions for SOA formation. Peng and Jimenez (2017) quantified the potential influence of NO on the oxidation chemistry by calculating the ratio of the reactive flux of the peroxy radicals with NO to the reactive flux of the peroxy radicals with HO_2 ($r_{RO_2+NO}/r_{RO_2+HO_2}$). A ratio greater than 1 was considered as "high NO" while a ratio less than 1 was considered "low NO". For the relative humidity, photon flux, initial NO, and external OH reactivity values in Jathar et al. (2017a), the model of Peng and Jimenez (2017) predicted that the OFR mostly ran in a high NO mode at all photochemical exposures when the engine was run at load conditions or with an aftertreatment device in place. However, the model predicted that the OFR mostly ran in a low NO mode especially at the high photochemical exposures when the engine was run at idle conditions and without an aftertreatment device (i.e., idle–diesel–none and idle–biodiesel–none). The $r_{RO_2+NO}/r_{RO_2+HO_2}$ ratio and low versus high NO mode for each photon flux and experiment combination is listed in Table S1 in the Supplement. Based on these results, we accordingly used the low and high NO_x parameterizations to perform the model simulations.

The model of Peng and Jimenez (2017) also indicated that most of the experiments performed by Jathar et al. (2017a) were run under, in what Peng and Jimenez (2017) refer to as, "risky" or "bad" conditions. These conditions refer to situations in the OFR where the initial NO concentrations and external OH reactivity are high enough to suppress OH exposure and lead to non-tropospheric photolysis at 185 and 254 nm, which could compete with OH exposure to determine the fate of the SOA precursors and its oxidation products. Such conditions could be avoided by ensuring low initial NO concentrations and external OH reactivity that for combustion emissions would require substantial dilution with clean air before they are oxidized in the OFR. Future studies on combustion sources should be cognizant of this fact to avoid artifacts linked to non-tropospheric photolysis of organic compounds in OFRs.

2.2 Organic aerosol models

In this work, we used two different OA models to predict the mass concentrations and chemical composition of SOA and compare predictions against the SOA measurements from Jathar et al. (2017a) and Friedman et al. (2017). In this section, we briefly describe the two model frameworks, namely the VBS and the SOM, used to simulate the coupled chemistry, thermodynamic properties, and kinetic gas–particle partitioning of OA. Neither model accounted for photolysis of organic compounds in the gas phase at 185 or 254 nm, which may need to be considered in the future when modeling the OFR chemistry from combustion emissions. The VBS model was chosen as it is widely used in contemporary air quality models; the SOM was chosen to examine the influence of improved representation of OA processes (e.g., fragmentation reactions) on model predictions.

2.2.1 Volatility basis set

The VBS model, developed by Donahue et al. (2006b), is a parameterizable model that allows for a volatility-based representation of the coupled chemistry, thermodynamic properties, and gas–particle partitioning of OA. The VBS uses logarithmically spaced so-called basis sets based on the effective

Table 1. Primary emissions of THC, CO, NO, NO_2, and POA, maximum photochemical production of SOA, maximum O : C of the OA, maximum OH exposure, and size distribution data from Jathar et al. (2017a).

Load–fuel–aftertreatment experiment	Date	THC ($\mu g\,m^{-3}$)	CO (ppbv)	NO (ppbv)	NO_2 (ppbv)	POA ($\mu g\,m^{-3}$)	SOA[a] ($\mu g\,m^{-3}$)	O : C[a]	OH exposure[a] (molec.-h cm^{-3})	Number mean dia.[b] (nm)	Number conc.[b] (cm^{-3})
Idle–diesel–none	3 June	1519	2746	960	318	38 ± 15	209 ± 66	0.23 ± 0.01	2.1×10^7	46	8.0×10^5
	5 June	1810	5809	878	502	35 ± 11	875 ± 288	0.46 ± 0.07	6.67×10^7		6.5×10^5
	12 June	2554	9664	1870	1103	85 ± 17	877 ± 277	0.57 ± 0.09	3.61×10^7		3.4×10^5
Idle–biodiesel–none	4 June	1118	4270	867	344	22 ± 12	999 ± 316	0.52 ± 0.07	9.17×10^7	46[c]	$7.3 \times 10^{5,c}$
	8 June	2160	8169	1578	811	69 ± 20	1415 ± 468	0.36 ± 0.03	4.72×10^7		$4.1 \times 10^{5,c}$
Load–diesel–none	3 June	959	1558	4999	379	19 ± 11	181 ± 58	0.37 ± 0.01	3.6×10^7	190	5.3×10^5
	5 June	711	1400	6690	34	37 ± 13	253 ± 100	0.32 ± 0.04	2.61×10^7		4.4×10^5
Load–biodiesel–none	4 June	1634	1410	6364	30	29 ± 18	645 ± 204	0.38 ± 0.05	2.78×10^7	190[c]	$5.0 \times 10^{5,c}$
	8 June	518	2051	10 813	496	46 ± 22	284 ± 106	0.30 ± 0.04	1.42×10^7		$3.3 \times 10^{5,c}$
Idle–diesel–DPF + DOC	9 June	2135	7473	2383	23	1.5 ± 0.6	1040 ± 335	0.37 ± 0.02	5×10^7		910
Load–diesel–DPF + DOC	9 June	303	85	6157	4483	1.6 ± 3.6	146 ± 48	0.29 ± 0.01	1.31×10^7	57	968
Idle–biodiesel–DPF + DOC	10 June	1773	7452	2213	182	2.6 ± 1	787 ± 250	0.44 ± 0.04	5.28×10^7	52[c]	910[c]
Load–biodiesel–DPF + DOC	10 June	261	58	5475	4525	2 ± 0.14	107 ± 9	0.29 ± 0.01	1.39×10^7	57[c]	968[c]

DPF is diesel particulate filter and DOC is diesel oxidation catalyst. [a] Maximum values measured in each experiment. [b] Values measured at no OH exposure. [c] No data, assumed to be similar to the equivalent diesel experiment for the model.

Table 2. SOA precursors and mass yields used in the VBS model for high NO_x conditions.

Species	$\log_{10}C^*$					Reference
	0.1	1	10	100	1000	
Toluene	0.0000	0.0100	0.2400	0.4500	0.7000	Hildebrandt et al. (2009)
Benzene	0.0392	0.0315	0.0000	0.8230	0.0957	Ng et al. (2007)[a]
m-Xylene	0.0032	0.0106	0.0633	0.0465	0.0000	Ng et al. (2007)[a]
p-Xylene	0.0000	0.0022	0.0764	0.0000	0.0000	Song et al. (2007)[a]
o-Xylene	0.0000	0.0132	0.1140	0.0000	0.0000	Song et al. (2007)[a]
Naphthalene	0.0000	0.1660	0.0000	0.5400	0.8130	Chan et al. (2009)[a]
1-Methylnaphthalene	0.0000	0.0170	0.4860	0.0000	0.0000	Chan et al. (2009)[a]
2-Methylnaphthalene	0.0000	0.0531	0.5040	0.0000	0.0000	Chan et al. (2009)[a]
1,2-Dimethylnaphthalene	0.0000	0.3100	0.0000	0.0000	0.0000	Chan et al. (2009)[a]
1-Methyl-3-n-propylbenzene	0.0000	0.0000	0.0405	0.0694	0.1140	Odum et al. (1996)[a]
n-Decane	0.0000	0.0000	0.0110	0.1280	0.2420	Presto et al. (2010)[b]
n-Undecane	0.0000	0.0040	0.0720	0.1760	0.1450	Presto et al. (2010)[b]
n-Dodecane	0.0000	0.0140	0.1100	0.1600	0.0000	Presto et al. (2010)
n-Tridecane	0.0140	0.0590	0.2200	0.4000	0.0000	Presto et al. (2010)
n-Tetradecane	0.0220	0.0940	0.3000	0.3500	0.0000	Presto et al. (2010)
n-Pentadecane	0.0440	0.0710	0.4100	0.3000	0.0000	Presto et al. (2010)
n-Hexadecane	0.0530	0.0830	0.4600	0.2500	0.0000	Presto et al. (2010)
n-Heptadecane	0.0630	0.0890	0.5500	0.2000	0.0000	Presto et al. (2010)

[a] Vapor wall losses are not accounted for. [b] Extrapolated from the Presto et al. (2010) data.

saturation concentration (C^*); C^* of a species determines the partitioning between the gas and particle phases (Pankow, 1994). In the VBS model, organic precursors were allowed to react with OH to yield a unique product distribution in C^* space that represented stable first-generation products. Subsequent multigenerational gas-phase oxidation, or so-called "aging", of the VBS products was modeled using the scheme of Robinson et al. (2007). In this scheme the product species are allowed to react with OH and yield a product with a C^* that is an order of magnitude lower than the direct precursor, to a lower limit C^* of 10^{-2} µg m^{-3}. This scheme did not consider fragmentation reactions. The following equations were used to represent the organic precursor oxidation (Eq. 1) and subsequent reaction and formation of products from the precursor oxidation and aging reactions (Eq. 2):

$$\frac{\mathrm{d}V}{\mathrm{d}t} = -k_{\mathrm{OH}}[V][\mathrm{OH}], \quad (1)$$

$$\frac{\mathrm{d}C_j^{\mathrm{g+p}}}{\mathrm{d}t} = \alpha_j k_{\mathrm{OH}}[V][\mathrm{OH}] + \beta k_{\mathrm{OH,aging}}\left[C_{j+1}^{\mathrm{g}}\right][\mathrm{OH}] - \gamma k_{\mathrm{OH,aging}}\left[C_j^{\mathrm{g}}\right][\mathrm{OH}], \quad (2)$$

where V is the gas-phase concentration of a generic organic precursor (µg m^{-3}; includes VOCs, IVOCs, and semivolatile VOCs), k_{OH} is the reaction rate constant between the precursor and OH (cm^3 molecule^{-1} s^{-1}), $C_j^{\mathrm{g+p}}$ is the gas + particle-phase concentration in the jth bin (µg m^{-3}), α_j is the mass yield of the first-generation oxidation product of the jth bin (Table 2), $k_{\mathrm{OH,aging}}$ is the reaction rate constant (cm^3 molecule^{-1} s^{-1}) to represent multigenerational aging of the oxidation products, and β and γ are the mass yields associated with the production and loss terms from multigenerational aging. For the jth bin, the second term in Eq. (2) represents the formation of oxidation products from the $j+1$th volatility bin and the third term in Eq. (2) represents the loss of precursor from the jth bin. β and γ are assumed to have a value of 1 (meaning no fragmentation) but β is 0 for the last bin and γ is 0 for the first bin.

Volatility-resolved mass yields for 18 different organic precursors for C^* bins ranging from 10^{-1} to 10^3 µg m^{-3} were adopted or refit based on low and high NO_x parameterizations published in the literature; organic precursors, the high and low NO_x VBS mass yields, and the relevant references are listed in Tables 2 and 3. High NO_x VBS mass yields for *n*-alkanes higher than *n*-heptadecane (*n*-octadecane, *n*-nonadecane, *n*-eicosane, *n*-heneicosane, *n*-docosane, and *n*-tricosane) were estimated from Presto et al. (2010), in which the mass yields were shifted by one C^* bin for an increase in two carbon numbers. Since there were no direct low NO_x VBS parameterizations for alkanes, parameterizations for linear, branched, and cyclic alkanes were developed using pseudo-chamber data generated with the SOM based on the low NO_x parameters listed in Table 5 for *n*-dodecane, methylundecane, and hexylcyclohexane, respectively (more details can be found in the Supplement). Some of these parameterizations accounted for vapor wall losses and have been accordingly marked in Tables 2 and 3. Each SOA precursor in the exhaust emissions was assigned a surrogate from Tables 2 and 3 to model SOA formation in the

Table 3. SOA precursors and mass yields used in the VBS model for low NO_x conditions.

Species	C^*					Reference
	0.1	1	10	100	1000	
Toluene	0.0000	0.0100	0.2400	0.7000	0.7000	Hildebrandt et al. (2009)
Benzene	0.3700	0.0000	0.0000	0.0000	0.0000	Ng et al. (2007)[a]
m-Xylene	0.3000	0.0000	0.0000	0.0000	0.0000	Ng et al. (2007)[a]
p-Xylene	0.0000	0.0022	0.0764	0.0000	0.0000	Song et al. (2007)[a]
o-Xylene	0.0000	0.0132	0.1145	0.0000	0.0000	Song et al. (2007)[a]
Naphthalene	0.7300	0.0000	0.0000	0.0000	0.0000	Chan et al. (2009)[a]
1-Methylnaphthalene	0.6800	0.0000	0.0000	0.0000	0.0000	Chan et al. (2009)[a]
2-Methylnaphthalene	0.5800	0.0000	0.0000	0.0000	0.0000	Chan et al. (2009)[a]
n-Decane	0.0002	0.0050	0.0013	0.3938	0.0278	Loza et al. (2014)[b]
n-Undecane	0.0001	0.0070	0.0216	0.3321	0.0000	Loza et al. (2014)[b]
n-Dodecane	0.0011	0.0080	0.0279	0.3902	0.0003	Loza et al. (2014)[b]
n-Tridecane	0.0029	0.0064	0.0551	0.3231	0.7090	Loza et al. (2014)[b]
n-Tetradecane	0.0004	1.2000	0.1777	0.0194	0.0014	Loza et al. (2014)[b]
n-Pentadecane	0.0032	0.0124	0.0686	0.5050	0.0025	Loza et al. (2014)[b]
n-Hexadecane	0.0000	0.0572	0.2754	0.4346	0.1710	Loza et al. (2014)[b]
n-Heptadecane	0.0399	0.0757	0.4409	0.3691	0.0000	Loza et al. (2014)[b]
n-Octadecane	0.1958	0.0203	0.7077	0.0777	0.0000	Loza et al. (2014)[b]
n-Nonadecane	1.0281	0.0000	0.0000	0.0000	0.0000	Loza et al. (2014)[b]
n-Eicosane	0.0024	0.8470	0.2160	0.0000	0.0000	Loza et al. (2014)[b]
n-Heneicosane	0.3629	0.6766	0.0250	0.0000	0.0000	Loza et al. (2014)[b]
n-Docosane	0.7991	0.2633	0.0000	0.0000	0.0000	Loza et al. (2014)[b]
C_{12} branched alkane	0.0077	0.0015	0.0416	0.2486	0.9179	Loza et al. (2014)[b]
C_{13} branched alkane	0.0105	0.0007	0.0610	0.2376	1.2045	Loza et al. (2014)[b]
C_{14} branched alkane	0.0135	0.0007	0.0819	0.4173	0.4879	Loza et al. (2014)[b]
C_{15} branched alkane	0.0156	0.0034	0.1677	0.3553	0.7973	Loza et al. (2014)[b]
C_{16} branched alkane	0.0075	0.0704	0.1689	0.5741	0.0000	Loza et al. (2014)[b]
C_{17} branched alkane	0.0510	0.0000	0.4527	0.4605	0.0000	Loza et al. (2014)[b]
C_{18} branched alkane	0.0836	0.0001	0.7962	0.1484	0.0000	Loza et al. (2014)[b]
C_{19} branched alkane	0.3151	0.0001	0.7470	0.0000	0.0000	Loza et al. (2014)[b]
C_{20} branched alkane	0.0198	0.8698	0.1725	0.0000	0.0000	Loza et al. (2014)[b]
C_{21} branched alkane	0.3753	0.6837	0.0000	0.0000	0.0000	Loza et al. (2014)[b]
C_{22} branched alkane	0.8517	0.2056	0.0000	0.0000	0.0000	Loza et al. (2014)[b]
C_{12} cyclic alkane	0.0128	0.0302	0.0124	0.6156	0.0043	Loza et al. (2014)[b]
C_{13} cyclic alkane	0.0297	0.0000	0.0939	0.4062	1.0776	Loza et al. (2014)[b]
C_{14} cyclic alkane	0.0322	0.0000	0.1521	0.5341	0.5717	Loza et al. (2014)[b]
C_{15} cyclic alkane	0.0345	0.0000	0.3430	0.3231	0.8672	Loza et al. (2014)[b]
C_{16} cyclic alkane	0.0147	0.1426	0.3616	0.2839	0.6597	Loza et al. (2014)[b]
C_{17} cyclic alkane	0.0574	0.2408	0.3453	0.4060	0.0000	Loza et al. (2014)[b]
C_{18} cyclic alkane	0.2546	0.0643	0.6091	0.1431	0.0000	Loza et al. (2014)[b]
C_{19} cyclic alkane	0.2940	0.2790	0.5010	0.0000	0.0000	Loza et al. (2014)[b]
C_{20} cyclic alkane	0.3423	0.5700	0.1653	0.0000	0.0000	Loza et al. (2014)[b]
C_{21} cyclic alkane	0.6100	0.4478	0.0155	0.0000	0.0000	Loza et al. (2014)[b]
C_{22} cyclic alkane	0.9573	0.1110	0.0013	0.0000	0.0000	Loza et al. (2014)[b]

[a] Vapor wall losses are not accounted for. [b] Produced from pseudo-chamber data generated using the SOM. For more details, refer to the Supplement.

VBS model. When using the high NO_x parameterizations, branched and cyclic alkanes were assigned surrogates based on equivalent linear alkanes, following the work of Lim and Ziemann (2009) and Tkacik et al. (2012). A C_X branched alkane was assigned a C_{X-2} linear alkane as a surrogate and a C_X cyclic alkane was assigned a C_{X+2} linear alkane as a surrogate. The idle–diesel–none and idle–biodiesel–none experiments used the low NO_x parameterizations while all

the other experiments used the high NO_x parameterizations. The mass transfer (condensation/evaporation) of the VBS products to the particle phase was assumed to be kinetically limited in the OFR (Palm et al., 2016; Jathar et al., 2017a; Ahlberg et al., 2017); Sect. 2.3 describes the mass transfer equation used to model kinetic gas–particle partitioning.

2.2.2 Statistical Oxidation Model

The SOM, developed by Cappa and Wilson (2012), is a semi-explicit, parameterizable model that allows for a statistical representation of the coupled chemistry, thermodynamic properties, and gas–particle partitioning of OA. The SOM uses a two-dimensional carbon–oxygen grid to track gas- and particle-phase precursors and products from precursor oxidation. Each cell in the SOM grid represents a model organic species with a molecular weight defined by the formula $C_x H_y O_z$. A SOM species reflects the average properties (e.g., C^*, reactivity) of all actual species with the same number of carbon (N_C) and oxygen (N_O) atoms that are produced from a given precursor class (e.g., benzene, alkanes). In the SOM, all gas-phase species are assumed to be reactive towards OH and the OH reaction rate constant (k_{OH}) is calculated using Eq. (3) as follows:

$$\log(k_{OH}) = A_1 + A_2 \times \left(N_C^{A_3}\right) \times \exp\left(-1 \times \frac{E_a}{8.314 \times T}\right) \times \left[1 + \frac{b_1}{\sigma\sqrt{2\pi}} \exp\left(-\frac{1\left(\ln(N_O + 0.01) - \ln(b_2)^2\right.}{2\sigma^2}\right)\right], \quad (3)$$

$$\sigma\,(N_C \le 15) = 0.0214 \times N_C + 0.5238,$$
$$\sigma\,(N_C \ge 15) = -0.115 \times N_C + 2.695,$$
$$b_1 = -0.2583 \times N_C + 5.8944,$$
$$b_2\,(N_C \le 15) = 0.0314 \times N_C + 0.9871,$$
$$b_2\,(N_C > 15) = 0.25 \times N_C - 2.183,$$

where $A_1 = 15.1$, $A_2 = 3.94$, and $A_3 = 0.797$. k_{OH} for a specified N_C and N_O is assumed to be the same for species in all the SOM grids.

The reactions with OH lead to either functionalization or fragmentation, resulting in movement through the carbon–oxygen grid. Six precursor-specific adjustable parameters are assigned for each SOM grid: four parameters that define the molar yields of the four functionalized, oxidized products ($p_{O,k}$, $\Sigma p_{O,k} = 1$ and hence one out of the four parameters is determined by mass balance), one parameter that determines the probability of functionalization or fragmentation (P_{Frag}, $P_{Func} = 1 - P_{Frag}$), and one parameter that describes the change in C^* associated with the addition of one oxygen atom (ΔLVP). Equation (4) represents the evolution of species in the SOM grid:

$$\frac{d[C_X O_Z]}{dt} = -k_{OH}^{X,Z}[OH][C_X O_Z] + [OH]\sum_{k=1}^{4} k_{OH}^{X,Z-k} P_{func}^{X,Z-k} p_{O,k}\left[C_X O_{Z-k}\right] + [OH]\sum_{j=1}^{j_{max}}\sum_{k=0}^{k_{max}-Z} k_{OH}^{X+j,Z-1+k} \frac{P_{frag}^{X,Z-1+k}}{N_{fragments}^{X,Z}}\left[C_X O_{Z-1+k}\right], \quad (4)$$

where $C_X O_Z$ is the gas + particle-phase concentration of the SOM species with X carbon atoms and Z oxygen atoms ($\mu g\,m^{-3}$) and $N_{fragments}$ is the number of possible products from fragmentation. The probability of fragmentation is modeled using Eq. (5) as a function of the O : C ratio because higher O : C ratio compounds are expected to have a higher probability of fragmentation (Chacon-Madrid and Donahue, 2011):

$$P_{frag} = \left(\frac{N_O}{N_C}\right)^{m_{frag}}. \quad (5)$$

The C^* for each SOM species was calculated using Eq. (6) as follows:

$$\log_{10} C^* = -0.337 MW_{HC} + 11.56 - (N_O \times \Delta LVP), \quad (6)$$

where MW_{HC} ($g\,mole^{-1}$) is the molecular weight of the hydrocarbon backbone (accounting only for the carbon and hydrogen atoms).

The parameters used to model SOA formation were based on those published in Cappa et al. (2016) and are listed in Tables 4 and 5. These parameter sets were developed by fitting the SOM predictions to chamber measurements of SOA mass concentrations and include corrections to account for vapor wall losses (Zhang et al., 2014). Each SOA precursor in the exhaust emissions was assigned a surrogate from Table 4 or 5 to account for the oxidation chemistry associated with oxidation of that species. For example, pentadecane used the parameterization developed by fitting *n*-dodecane. The difference in the initial number of carbons and oxygens, and thus the volatility, between the surrogate compound and the precursor compound of interest was accounted for, with consequent impact on the SOA yield. In other words, unlike the VBS where the SOA mass yield of the SOA precursor and surrogate is identical, the surrogate in the SOM only informed the statistical trajectory for multigenerational oxidation of a given precursor, and the surrogate and actual compound of interest can have different SOA mass yields. The idle–diesel–none and idle–biodiesel–none experiments used the low NO_x parameters while all the other experiments used the high NO_x parameters. Similar to the VBS model, the mass transfer (condensation/evaporation) of the SOM products to the particle phase was assumed to be kinetically limited in the OFR (Palm et al., 2016; Jathar et al.,

Table 4. SOA precursors and parameters used in the SOM (Cappa et al., 2016) for high NO_x conditions.

Species	m_{frag}	ΔLVP	$p_{O,1}$	$p_{O,2}$	$p_{O,3}$	$p_{O,4}$	Reference
n-Dodecane	0.0980	1.3900	0.9270	0.0101	0.0180	0.0445	Loza et al. (2014)
Methylundecane	0.0100	1.2100	0.7419	0.0011	0.1820	0.0750	Loza et al. (2014)
Hexylcyclohexane	0.0477	1.5700	0.7313	0.0381	0.2101	0.0205	Loza et al. (2014)
Toluene	0.2220	1.2400	0.0029	0.0010	0.0010	1.0100	Zhang et al. (2014)
Benzene	0.5350	1.7000	0.0792	0.0010	0.9190	0.0010	Ng et al. (2007)
m-Xylene	0.0100	1.6800	0.9360	0.0010	0.0021	0.0609	Ng et al. (2007)
Naphthalene	0.1210	1.3100	0.6440	0.0010	0.0460	0.3080	Chan et al. (2009)

Table 5. SOA precursors and parameters used in the SOM (Cappa et al., 2016) for low NO_x conditions.

Species	m_{frag}	ΔLVP	$p_{O,1}$	$p_{O,2}$	$p_{O,3}$	$p_{O,4}$	Reference
n-Dodecane	2.0000	1.8300	0.9990	0.0010	0.0010	0.0010	Loza et al. (2014)
Methylundecane	2.8200	1.9100	0.9980	0.0010	0.0010	0.0010	Loza et al. (2014)
Hexylcyclohexane	5.0000	2.0500	0.8160	0.1810	0.0019	0.0010	Loza et al. (2014)
Toluene	1.3100	1.7700	0.1850	0.0010	0.0019	0.8120	Zhang et al. (2014)
Benzene	0.0807	1.9700	0.6370	0.0010	0.0021	0.3600	Ng et al. (2007)
m-Xylene	1.0800	2.0500	0.1020	0.0010	0.8780	0.0190	Ng et al. (2007)
Naphthalene	0.1890	1.8700	0.3520	0.0543	0.5330	0.0609	Chan et al. (2009)

2017a; Ahlberg et al., 2017) and Sect. 2.3 below describes the mass transfer equation used to model kinetic gas–particle partitioning.

2.3 Kinetic gas–particle partitioning

Palm et al. (2016), Ahlberg et al. (2017), and Jathar et al. (2017a) have argued that the short residence times and small condensation sinks in the OFR may not permit all low-volatility products formed from precursor oxidation to condense onto preexisting aerosol. Hence, unlike earlier work that has assumed equilibrium partitioning to model SOA in OFRs (Tkacik et al., 2014; Chen et al., 2013), we modeled the kinetic gas–particle partitioning of OA using Eq. (7) (Zhang et al., 2014):

$$\frac{\mathrm{d}C_i^{\mathrm{p}}}{\mathrm{d}t} = 2\pi\, D_i\, D_{\mathrm{p}} N_{\mathrm{p}} F_{\mathrm{FS}} \left(C_i^{\mathrm{g}} - \frac{C_i^{\mathrm{p}} C_i^*}{C_{\mathrm{OA}}} \right), \tag{7}$$

where C_i^{p} is the particle-phase mass concentration for the ith organic species ($\mu g\, m^{-3}$), D_i is the gas-phase diffusion coefficient of the ith organic species ($m^2\, s^{-1}$), D_{p} is the number mean particle diameter (m), N_{p} is the total particle number concentration (m^{-3}), F_{FS} is Fuchs–Sutugin correction for non-continuum mass transfer, C_i^{g} is the gas-phase mass concentration of the ith organic species ($\mu g\, m^{-3}$), C_i^* is the effective saturation concentration of the ith organic species, and C_{OA} is the total OA mass concentration ($\mu g\, m^{-3}$). The ith organic species refers to the organic compounds tracked in the VBS bins and the SOM grids. The gas-phase diffusion coefficient was calculated for each organic species as follows:

$$D_i = D_{\mathrm{CO_2}} \frac{\mathrm{MW_{CO_2}}}{\mathrm{MW}_i}, \tag{8}$$

where $D_{\mathrm{CO_2}}$ is the gas-phase diffusion coefficient of CO_2 ($1.38 \times 10^{-5}\, m^2\, s^{-1}$), $\mathrm{MW_{CO_2}}$ ($g\, mole^{-1}$) is the molecular weight of CO_2, and MW_i ($g\, mole^{-1}$) is the molecular weight of the ith organic species. In the VBS model where we do not track the molecular composition of the SOA species, we assumed all condensing species to have a molecular weight of $200\, g\, mole^{-1}$. This formulation to calculate the gas-phase diffusion coefficient underpredicted the measured gas-phase diffusion coefficients compiled by Tang et al. (2015) by $\sim 20\,\%$. However, doubling the gas-phase diffusion coefficient calculated in Eq. (8) resulted in very small change ($< 1\,\%$) in the OA mass predictions for a representative experiment. Hence, we decided to use the formulation in Eq. (8) for the rest of this work. The Fuchs–Sutugin correction was calculated as follows:

$$F_{\mathrm{FS}} = \frac{0.75\alpha(1+Kn)}{Kn^2 + Kn + 0.283 \cdot Kn \cdot \alpha + 0.75\alpha}, \tag{9}$$

$$Kn = \frac{2\lambda_i}{D_{\mathrm{p}}}, \tag{10}$$

$$\lambda_i = \frac{3D_i}{C_j}, \tag{11}$$

$$C_i = \sqrt{\frac{8N_{\mathrm{A}}kT}{\pi \mathrm{MW}_i}}, \tag{12}$$

where Kn is the Knudsen number, α is the mass accommodation coefficient, λ_i is the mean free path of the ith organic

Table 6. **(a)** Volatility- and **(b)** carbon-number resolved distributions used to determine mass concentrations of POA in the VBS and SOM models, respectively. The volatility distributions are from May et al. (2013b).

(a)									
C^* ($\mu g\,m^{-3}$)	10^{-2}	10^{-1}	10^{1}	10^{2}	10^{3}	10^{4}	10^{5}	10^{6}	
f_i	0.03	0.25	0.37	0.23	0.06	0.03	0.01	0.01	

(b)													
Carbon no.	< 16	16	17	18	19	20	21	22	23	24	25	26	> 26
f_i	0.003	0.000	0.058	0.043	0.055	0.094	0.146	0.181	0.178	0.137	0.078	0.026	0.001

species in air (m), C_i is the root mean square speed of the gas ($m\,s^{-1}$), N_A is Avogadro's number ($molecules\,mole^{-1}$), k is the Boltzmann constant ($m^2\,kg\,s^{-2}\,K^{-1}$), and T is the temperature (K).

2.4 Model inputs

2.4.1 Semi-volatile and reactive POA

Previous work has shown that much of combustion-related POA is semi-volatile and exists in an equilibrium with gas-phase vapors (Robinson et al., 2007; Huffman et al., 2009; May et al., 2013a–c). Jathar et al. (2017a) measured emissions of POA at no OH exposure and these measured concentrations were used to initialize the seed OA available for partitioning in the OFR and to calculate the mass concentrations of vapors in equilibrium with the POA. The mass concentrations of the POA vapors were determined based on the normalized, volatility-resolved distribution of primary organic compounds estimated by May et al. (2013b) for emissions from a suite of on- and off-road diesel vehicles. The volatility distribution of May et al. (2013b) for diesel primary organic compounds is listed in Table 6a. For the SOM, we assumed that the primary organic compounds could be represented using a distribution of n-alkanes and we refit the volatility distribution in Table 6a to develop a carbon-number resolved distribution of n-alkanes; this distribution is listed in Table 6b.

2.4.2 SOA precursors

Jathar et al. (2017a) did not speciate the THC or SOA precursor emissions from the diesel engine and hence we have developed our own emissions profiles based on previously published literature to speciate the THC emissions. In this work, we used two different emissions profiles listed in EPA SPECIATE version 4.3 that are commonly used to speciate THC emissions from diesel engines for emissions inventories used in atmospheric modeling (EPA, 2011): profiles 3161 (diesel exhaust – farm equipment) and 8774 (heavy duty diesel exhaust). Profile 3161 best matched the diesel engine source and diesel fuel used by Jathar et al. (2017a) and was used as the baseline emissions profile to speciate the THC emissions; we examined the sensitivity of using Profile 8774 on model predictions. We were unable to find a comprehensive emissions profile for THC emissions from the use of straight biodiesel fuel in the literature and have relied on emissions profiles that were determined for biodiesel-diesel blends. Profile 4777 (30 % biodiesel exhaust – light duty truck) was used as the baseline emissions profile to speciate THC emissions for experiments performed using the biodiesel fuel. All three emissions profiles (3161, 8774, and 4777) are listed in Tables S2 through S4.

Prior work in studying SOA formation has revealed that traditional speciation of THC emissions does not include emissions of high molecular-weight organic compounds, such as IVOCs, that are important SOA precursors (Jathar et al., 2014b). In Profile 3161 such compounds are partially accounted for in the "unknown" species category (13.76 % by mass of THC). Zhao et al. (2015) recently estimated that IVOCs were 60 % of the THC emissions from a suite of on- and off-road diesel engines and provided a semi-explicit speciation of the IVOC emissions as a carbon-number distribution of linear, branched, and cyclic alkanes. To account for these IVOC emissions, we assumed that the base case emissions profiles contained 30 % IVOCs on a mass basis (this IVOC fraction was selected since it resulted in the most optimum model–measurement comparison for OA mass; this will be discussed later in Sect. 3.3) and had the same chemical speciation as that proposed by Zhao et al. (2015) for an off-road engine (transportation refrigeration unit). We performed sensitivity simulations using IVOC fractions of 0 % (assuming that the THC emissions contained no IVOCs), 13.76 % (based on the "unknown" category in Profile 3161), and 60 % (based on the median estimate in Zhao et al., 2015), on a mass basis. Addition of IVOCs to the emissions profile meant that the VOC species (e.g., benzene, toluene, short alkanes) had to be renormalized to accommodate the IVOCs. Table 7 lists the renormalized baseline emissions profiles for SOA precursors used for diesel and biodiesel exhaust with 30 % IVOCs along with the reaction rate constants with OH (k_{OH}) and surrogates (or model compound) used to model SOA formation for the VBS and SOM models. Con-

centrations for each species were determined by multiplying the experiment-specific THC mass concentrations with the renormalized emissions profiles.

2.4.3 Particle size and particle number concentrations

For numerical simplicity, we used a monodisperse aerosol, the properties of which (number mean diameter, D_p; number concentration, N_p) were initialized from the measured particle size distribution data when modeling kinetic gas–particle partitioning. For experiments performed without the DPF + DOC, the initial particle number concentrations and condensational sinks were high ($> 3.3 \times 10^5\,cm^{-3}$ and $> 0.5\,min^{-1}$) and hence the monodisperse aerosol was initialized based on data at no photochemical exposure. For experiments performed with the DPF + DOC where the initial particle number concentrations were relatively low ($< 1000\,cm^{-3}$ and $< 0.003\,min^{-1}$), photochemical aging resulted in formation and growth of new particles and provided a substantial increase in the surface area (> factor of 300) available for condensation. In these experiments, we initialized the monodisperse aerosol using an average of the data at no photochemical exposure and after photochemical exposure (Palm et al., 2016). Averaging the data allowed for a more realistic estimate of the condensational sink. In each simulation, the condensing SOA mass was used to calculate the change in particle size but the number concentration was conserved. The number mean diameter and the number concentration data – representing the initial condensational sink – for all experiments are listed in Table 1.

New particle formation and growth was observed for most experiments at or near the highest photochemical ages (at or > 1 OH day), which presumably influenced the condensational sink at the beginning of the experiment. Therefore, we performed sensitivity simulations to investigate the influence of new particle formation on model predictions. We performed simulations with each model (VBS and SOM) with four different initial condensational sinks. The first three simulations used measured data to calculate the initial condensational sink inputs: (i) number mean diameter and measured number concentration at no OH exposure (equivalent to the default for non-DPF + DOC experiments), (ii) number mean diameter and measured number concentration at the given OH exposure, and (iii) average of (i) and (ii) (default for DPF + DOC experiments). The fourth simulation (iv) assumed that the OFR nucleated 1 nm particles at the beginning of the experiment where the number concentration of these particles was equal to that measured at the end of the experiment.

2.5 Model simulations and model code

The VBS and SOM models were run separately for each photochemical exposure simulated for each experiment listed in Table 1. In the VBS simulations, POA was tracked in one basis set while products from each SOA precursor were tracked in separate basis sets, allowing us to distinguish between POA and SOA. In the SOM simulations, all precursor molecules with the same surrogate (e.g., all *n*-alkanes) were tracked in the same SOM grid. Model simulations were performed in phases to answer specific questions and inform model inputs for later simulations:

1. To provide a general overview of the model predictions and model–measurement comparison, and to orient the reader to the results thereafter, we performed simulations with the VBS and SOM models using the base set of inputs for one of the idle–diesel–none experiments. Our base case included Profile 3161 for VOC emissions, 30 % IVOC mass fraction, kinetic gas–particle partitioning with a mass accommodation coefficient of 0.1, and monodisperse aerosol inputs based on measured data at no photochemical exposure. The partitioning- and IVOC-related choices for the base case are discussed in Sects. 3.2 and 3.3, respectively.

2. Models used to simulate SOA production in environmental chambers and OFRs have typically assumed instantaneous equilibrium partitioning (e.g., Chen et al., 2013). To examine the validity of assuming instantaneous equilibrium partitioning, we performed simulations with the VBS and SOM models using instantaneous or kinetic gas–particle partitioning for one of the idle–diesel–none and the idle–diesel–DPF + DOC experiments. Kinetic partitioning was modeled using three values of the mass accommodation coefficient ($\alpha = 0.01$, 0.1, 1) to capture the uncertainty in its true value. To examine the influence of an increased initial condensational sink from new particle formation on kinetic partitioning, we performed additional simulations using four different initial condensational sinks (see Sect. 2.4.3) on one of the idle–diesel–none and the idle–diesel–DPF + DOC experiments.

3. Previous work has shown that combustion-related IVOCs are important precursors of SOA (e.g., Jathar et al., 2014b). To investigate the importance of IVOCs, we performed simulations with the VBS and SOM models at four different assumed IVOC mass fractions (0, 13.76, 30, and 60 %), as discussed above when discussing the THC profiles, at all photochemical exposures and for all the experiments listed in Table 1. We performed additional simulations with different emissions profiles and SOA parameterizations on one of the idle–diesel–none experiments to investigate uncertainties linked to the composition and SOA potential of IVOCs.

4. Additional simulations were performed to examine the sensitivity of model predictions to the following processes: multigenerational aging, vapor wall losses, res-

Table 7. Reaction rate constants (k_{OH}), mass fractions, and VBS and SOM surrogates for SOA precursors in diesel and biodiesel emissions. k_{OH} values are from Atkinson and Arey (2003) when available or the EPI Suite version 4.11 (EPA, 2017). n/a = not applicable.

Species	Carbon number	k_{OH} (cm^3 $molecules^{-1}$ s^{-1})	Mass percentage of THC		VBS surrogate	SOM surrogate
			Diesel	Biodiesel		
Ethylbenzene	8	7.0×10^{-12}	0.2516	0.0826	Toluene	Toluene
Indan	9	1.9×10^{-11}	0.1542	n/a	Naphthalene	Naphthalene
Butylbenzene	10	4.5×10^{-12}	0.0081	0.4720	*m*-Xylene	*m*-Xylene
Diethylbenzene	10	8.11×10^{-12}	0.0731	n/a	*m*-Xylene	*m*-Xylene
Isopropyltoluene	10	8.54×10^{-12}	n/a	0.3599	Toluene	Toluene
m-Xylene	8	2.31×10^{-11}	0.4951	0.3717	*m*-Xylene	*m*-Xylene
o-Xylene	8	1.36×10^{-11}	0.2760	0.3953	*o*-Xylene	*m*-Xylene
p-Xylene	8	1.43×10^{-11}	0.0812	n/a	*p*-Xylene	*m*-Xylene
n-Decane	10	1.1×10^{-11}	0.4302	1.7050	*n*-Decane	*n*-Decane
n-Undecane	11	1.23×10^{-11}	0.2110	1.9410	*n*-Undecane	*n*-Dodecane
Toluene	7	5.63×10^{-12}	1.1932	1.6401	Toluene	Toluene
n-Tridecane	13	1.68×10^{-11}	n/a	0.6136	*n*-Tridecane	*n*-Dodecane
Benzaldehyde	7	1.2×10^{-11}	0.5682	n/a	Benzene	Benzene
Benzene	6	1.22×10^{-12}	1.6234	1.5988	Benzene	Benzene
C_{10} aromatics	10	2.3×10^{-11}	0.0649	n/a	*m*-Xylene	*m*-Xylene
C_9 aromatics	9	2.31×10^{-11}	0.4058	n/a	*m*-Xylene	*m*-Xylene
1,2,3-Trimethylbenzene	9	3.27×10^{-11}	0.0974	n/a	*m*-Xylene	*m*-Xylene
1,2,4-Trimethylbenzene	9	3.25×10^{-11}	0.4302	0.4720	*m*-Xylene	*m*-Xylene
1,2-Diethylbenzene	10	8.11×10^{-12}	0.0731	n/a	Toluene	Toluene
1,3,5-Trimethylbenzene	9	5.67×10^{-11}	n/a	0.1888	*m*-Xylene	*m*-Xylene
1,2-Dimethyl-4-ethylbenzene	10	1.69×10^{-11}	n/a	0.176	*m*-Xylene	*m*-Xylene
1,3-Dimethyl-2-ethylbenzene	10	1.76×10^{-11}	n/a	0.3304	*m*-Xylene	*m*-Xylene
1,4-Dimethyl-2-ethylbenzene	10	1.69×10^{-11}	n/a	0.4366	*m*-Xylene	*m*-Xylene
1-(1,1-dimethylethyl)-3,5-dimethylbenzene	12	3.01×10^{-11}	n/a	0.3717	*m*-Xylene	*m*-Xylene
1-Methyl-2-ethylbenzene	9	7.44×10^{-12}	0.1136	0.3835	Toluene	Toluene
1-Methyl-3-ethylbenzene	9	1.39×10^{-11}	0.2029	0.7198	Toluene	Toluene
1-Methyl-2-tert-butylbenzene	11	6.74×10^{-12}	n/a	0.4307	Toluene	Toluene
1-Tert-butyl-4-ethylbenzene	12	7.42×10^{-12}	n/a	0.1947	*m*-Xylene	*m*-Xylene
2-Methyl-butyl-benzene	11	1.02×10^{-11}	n/a	1.1032	*m*-Xylene	*m*-Xylene
3,3-Dimethyloctane	10	7.21×10^{-12}	n/a	0.3068	*n*-Decane	Methylundecane
3-Ethyloctane	10	1.18×10^{-11}	n/a	0.1888	*n*-Decane	Methylundecane
3-Methylnonane	10	1.14×10^{-11}	n/a	0.2655	*n*-Decane	Methylundecane
C_{12} branched alkane	12	1.82×10^{-11}	1.1335	1.1335	*n*-Decane	Methylundecane
C_{13} branched alkane	13	1.68×10^{-11}	0.8111	0.8111	*n*-Undecane	Methylundecane
C_{14} branched alkane	14	1.39×10^{-11}	0.5257	0.5257	*n*-Dodecane	Methylundecane
C_{15} branched alkane	15	1.82×10^{-11}	0.4692	0.4692	*n*-Tridecane	Methylundecane
C_{16} branched alkane	16	1.96×10^{-11}	0.4935	0.4935	*n*-Tetradecane	Methylundecane
C_{17} branched alkane	17	2.1×10^{-11}	0.2198	0.2198	*n*-Pentadecane	Methylundecane
C_{18} branched alkane	18	2.24×10^{-11}	0.2863	0.2863	*n*-Hexadecane	Methylundecane
C_{19} branched alkane	19	2.38×10^{-11}	0.1716	0.1716	*n*-Heptadecane	Methylundecane
C_{20} branched alkane	20	2.52×10^{-11}	0.0969	0.0969	*n*-Octadecane	Methylundecane
C_{21} branched alkane	21	2.67×10^{-11}	0.0639	0.0639	*n*-Nonadecane	Methylundecane
C_{22} branched alkane	22	2.81×10^{-11}	0.0604	0.0604	*n*-Eicosane	Methylundecane
C_{12} cyclic alkane	12	1.82×10^{-11}	4.3427	4.3427	*n*-Tetradecane	Hexylcyclohexane
C_{13} cyclic alkane	13	1.68×10^{-11}	4.4265	4.4265	*n*-Pentadecane	Hexylcyclohexane
C_{14} cyclic alkane	14	1.39×10^{-11}	3.1480	3.1480	*n*-Hexadecane	Hexylcyclohexane
C_{15} cyclic alkane	15	1.82×10^{-11}	2.8599	2.8599	*n*-Heptadecane	Hexylcyclohexane
C_{16} cyclic alkane	16	1.96×10^{-11}	2.1848	2.1848	*n*-Octatadecane	Hexylcyclohexane
C_{17} cyclic alkane	17	2.1×10^{-11}	1.8546	1.8546	*n*-Nonadecane	Hexylcyclohexane
C_{18} cyclic alkane	18	2.24×10^{-11}	1.6900	1.6900	*n*-Eicosane	Hexylcyclohexane
C_{19} cyclic alkane	19	2.38×10^{-11}	1.0570	1.0570	*n*-Heneicosane	Hexylcyclohexane
C_{20} cyclic alkane	20	2.52×10^{-11}	0.5900	0.5900	*n*-Docosane	Hexylcyclohexane
C_{21} cyclic alkane	21	2.67×10^{-11}	0.3736	0.3736	*n*-Tricosane	Hexylcyclohexane
C_{22} cyclic alkane	22	2.81×10^{-11}	0.3141	0.3141	*n*-Tricosane	Hexylcyclohexane

Table 7. Continued.

Species	Carbon number	k_{OH} (cm^3 molecules^{-1} s^{-1})	Mass percentage of THC		VBS surrogate	SOM surrogate
			Diesel	Biodiesel		
Dodecane	12	1.82×10^{-11}	0.5830	0.5830	*n*-Dodecane	*n*-Dodecane
Tridecane	13	1.68×10^{-11}	0.5465	0.5465	*n*-Tridecane	*n*-Dodecane
Tetradecane	14	1.39×10^{-11}	0.3649	0.3649	*n*-Tetradecane	*n*-Dodecane
Pentadecane	15	1.82×10^{-11}	0.3063	0.3063	*n*-Pentadecane	*n*-Dodecane
Hexadecane	16	1.96×10^{-11}	0.2281	0.2281	*n*-Hexadecane	*n*-Dodecane
Heptadecane	17	2.1×10^{-11}	0.1655	0.1655	*n*-Heptadecane	*n*-Dodecane
Octadecane	18	2.24×10^{-11}	0.1481	0.1481	*n*-Octatadecane	*n*-Dodecane
Nonadecane	19	2.38×10^{-11}	0.0726	0.0726	*n*-Nonadecane	*n*-Dodecane
Eicosane	20	2.52×10^{-11}	0.0365	0.0365	*n*-Eicosane	*n*-Dodecane
Heneicosane	21	2.67×10^{-11}	0.0222	0.0222	*n*-Heneicosane	*n*-Dodecane
Docosane	22	2.81×10^{-11}	0.0143	0.0143	*n*-Docosane	*n*-Dodecane
Pristane	19	2.44×10^{-11}	0.1434	0.1434	*n*-Nonadecane	Methylundecane
Phytane	20	2.61×10^{-11}	0.0799	0.0799	*n*-Eicosane	Methylundecane
Naphthalene	10	2.3×10^{-11}	0.1038	0.1038	Naphthalene	Naphthalene
Phenanthrene	14	1.3×10^{-11}	0.0117	0.0117	Naphthalene	Naphthalene

idence time distributions, and spatial heterogeneity in OH concentrations.

The numerical codes for the VBS were developed in MATLAB while those for the SOM were developed in IGOR (WaveMetrics Inc.). These codes will be made available on request. The simulations were performed on an Intel i5 processor (1.7 GHz) and required ∼ 10 s to perform a VBS simulation and ∼ 500 s to perform a SOM simulation at a single photochemical exposure.

3 Results

3.1 General model results using the base case

In Fig. 1, we compare predictions of OA from the VBS and SOM models using the base case to the measurements for the idle–diesel–none experiment performed on 5 June. Figure 1a and b compare predictions to the measurements in units of μg m^{-3} and g kg-fuel^{-1}, respectively; hereafter we present all mass predictions in units of g kg-fuel^{-1}. For this experiment, the VBS and SOM models overpredicted the OA mass by a factor of 2.0 and 2.2 at the lowest photochemical exposure (0.06 OH days) and a factor of 1.6 and 1.8 at the next highest photochemical exposure (0.17 OH days), respectively. The overprediction was because the models significantly overpredicted the SOA formation at these two photochemical exposures. For higher photochemical exposures (> 0.5 OH days), both models slightly underpredicted the OA mass but predictions were still within the measurement uncertainty. Our base case seemed to offer a mixed model–measurement comparison for this specific experiment (i.e., overprediction at lower photochemical ages and a slight underprediction at higher photochemical ages)

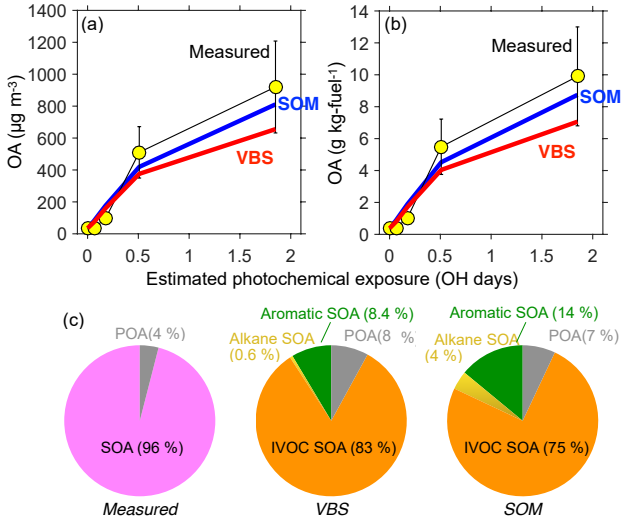

Figure 1. VBS and SOM model predictions of OA compared to measurements from the experiment performed on 5 June (idle–diesel–none) as a function of photochemical age. Inputs for both models have been specified in the text. Panel **(a)** has comparisons in μg m^{-3} and panel **(b)** has comparisons in g kg-fuel^{-1}. Panel **(c)** shows the modeled and measured OA composition at the highest photochemical exposure.

because the 30 % IVOC mass fraction used in the base case was optimized to achieve a favorable model–measurement comparison across all experiments at all photochemical exposures. In other words, the overprediction in this experiment at lower photochemical exposures was probably offset by an underprediction at similar photochemical exposures for some of the other experiments. It is important to note

that the model performance varied across the suite of experiments and this overall model performance is discussed in more detail in Section 3.3. The VBS and SOM models predicted that the OA at the maximum photochemical exposure was dominated by SOA produced from VOC and IVOC oxidation (92–93 %), which agreed well with the measured composition (see Fig. 1c). For the measurements, POA was defined as fresh OA while SOA was defined as OA formed in addition to the POA. Furthermore, both models suggested that most of the SOA emanated from the oxidation of IVOCs with only 8.6–14 % resulting from the oxidation of aromatic VOCs and less than 0.6–4 % resulting from alkane VOCs smaller than a C_{12}. This dominance of IVOCs in explaining the photochemically produced SOA is in line with previous OFR and chamber studies that have modeled SOA formation from diesel exhaust (Tkacik et al., 2014; Zhao et al., 2015; Jathar et al., 2014b).

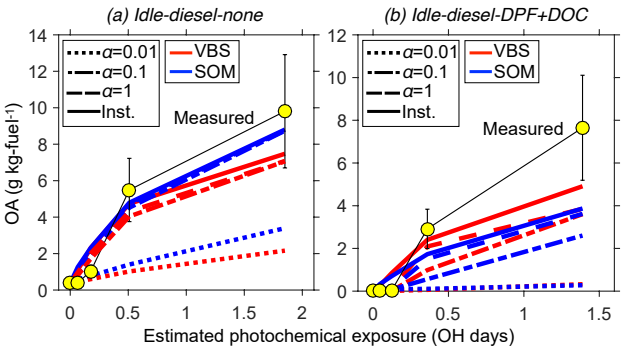

Figure 2. VBS model predictions of OA compared to measurements from the experiment performed on 5 June (idle–diesel–none) as a function of photochemical age assuming instantaneous equilibrium partitioning and kinetic gas–particle partitioning run at three accommodation coefficients: $\alpha = 1$ (dash-dot), 0.1 (dash), and 0.01 (solid).

3.2 Kinetic gas–particle partitioning

In Fig. 2, we plot predictions from the VBS and SOM models for the idle–diesel–none and idle–diesel–DPF + DOC experiments assuming instantaneous and kinetic gas–particle partitioning. The two different experiments were deliberately chosen to highlight the role instantaneous partitioning plays at the extremities. We found that for the idle–diesel–none experiment, the use of instantaneous partitioning roughly produced the same result as kinetic partitioning with α values of 0.1 and 1 and that all these predictions resulted in roughly the same model–measurement comparison. The instantaneous partitioning predictions were slightly higher than the kinetic partitioning predictions for the VBS simulations. The kinetic partitioning simulations (except for that with an α of 0.01) produced the same result as the instantaneous partitioning simulation most likely because the initial condensational sink was large enough ($1.12\,\mathrm{min}^{-1}$) in this experiment that there were no kinetic limitations to partitioning. The increase in the condensational sink through condensation of SOA ($10\,\mathrm{min}^{-1}$ at the highest photochemical exposure) tended to further reduce any differences in the predictions between the kinetic and instantaneous partitioning simulations. However, for the idle–diesel–DPF + DOC experiment, the instantaneous partitioning simulations predicted substantial OA mass at the lower photochemical exposures (0.04 and 0.12 OH days) compared to the kinetic partitioning simulations, specifically a factor of 9.8–29 larger at 0.04 OH days and a factor of 9.7–75 larger at 0.12 OH days for the VBS model and a factor of 3.9–5.8 larger at 0.04 OH days and a factor of 6.4–9.1 larger for the SOM. The instantaneous partitioning simulations consequently overpredicted the measurements while the kinetic partitioning simulations were more in line with the measurements. The instantaneous partitioning simulations predicted a lot more SOA because all condensable products of organic precursor oxidation were allowed to condense instantaneously (according to their respective volatilities) while the kinetic partitioning simulations predicted little SOA production because the initial condensational sink was quite small ($0.002\,\mathrm{min}^{-1}$). Predictions from the instantaneous and kinetic partitioning simulations were much closer at the higher photochemical exposures because the SOA formed had grown the condensational sink enough to reduce limitations to partitioning ($1\,\mathrm{min}^{-1}$ at the highest photochemical exposure). These results imply that the condensation of SOA in OFRs, in some instances, could be kinetically limited and that instantaneous partitioning may result in models overpredicting the condensation and formation of SOA.

We make two additional observations based on the results in Fig. 2. First, the initial condensational sink for the idle–diesel–none experiment was large ($1.12\,\mathrm{min}^{-1}$) compared to condensational sinks one would encounter in the real atmosphere. For example, $5\,\mu\mathrm{g\,m}^{-3}$ of aerosol in a representative rural or remote environment will have a condensational sink $< 0.05\,\mathrm{min}^{-1}$ (Seinfeld and Pandis, 2006). Therefore, modeling ambient applications of the OFR or OFR use with sources that use emissions control devices will need to be even more mindful of the instantaneous partitioning assumption while predicting SOA formation. Second, for the kinetic partitioning results, predictions from both models were relatively less sensitive to α values between 0.1 and 1 but were dramatically lower for an α value of 0.01 – more than a factor of 2 for the idle–diesel–none experiment and more than an order of magnitude for the idle–diesel–DPF + DOC experiment. Given the low sensitivity to α values greater than 0.1 and the reasonable model–measurement comparison at an α value of 0.1 and 1 at least for the idle–diesel–none experiment, we argue that the SOA condensation can be represented by an α value larger than 0.1 for the OFR experiments in this work. This α value for diesel exhaust SOA was consistent with prior estimates of the α value for biogenic SOA estimated from chamber, OFR, and aerosol heating ex-

periments (Lee et al., 2011; Saleh et al., 2013; Karnezi et al., 2014; Palm et al., 2016) and direct measurements of α for alkanol SOA (Krechmer et al., 2017). However, an α of 0.1 was an order of magnitude higher than that observed recently for toluene SOA under dry conditions (Zhang et al., 2014). Model results presented hereafter include a kinetic treatment of gas–particle partitioning and assumed a mass accommodation coefficient of 0.1.

Results from model simulations performed using different initial condensational sink inputs, some of which captured the influence of new particle formation, are plotted in Fig. 3. We found that the initial condensational sink had no influence on the OA predictions from both models for the idle–diesel–none experiment, despite substantial differences in the initial condensational sink between the different cases. This was because the amount of SOA formed (920 $\mu g\,m^{-3}$ at the highest photochemical exposure) was sufficient to grow the condensational sink enough that the initial condensational sink did not matter. In contrast, for both models we found large differences between the model predictions of OA for the idle–diesel–DPF + DOC experiment. The use of inputs based on the measurements at no OH exposure, where the aftertreatment system significantly reduced number concentrations (910 cm^{-3}) and hence the available condensational sink (0.002 min^{-1}), produced much less SOA (an order of magnitude lower or more) and poorer agreement with the measurements – see curve (i) in Fig. 3b. Initial condensational sinks that captured the influence of new particle formation resulted in higher model predictions but were still about a factor of ∼ 2 lower for the VBS simulations and a factor of ∼ 2.7 lower for the SOM simulations when compared against the measurements. The DPF + DOC results also suggest that calculating an initial condensational sink using data from before and after the photochemical exposure, as done by Palm et al. (2016), could be used as an input to model OFR data. Slight differences between the different curves for the idle–diesel–none experiment and curves (ii)–(iv) for the idle–diesel–DPF + DOC experiment can be attributed to the interaction of multigenerational aging and kinetic gas–particle partitioning.

3.3 Influence of IVOCs on SOA formation

In Fig. 4a, we compare predictions of SOA concentrations from the SOM against measurements for all the experiments listed in Table 1 and at all photochemical exposures. For visual clarity, we do not present results from the VBS model as both models had nearly identical predictions with a few exceptions. The panels in Fig. 4 show model–measurement comparisons assuming four different fractions of IVOCs: 0, 13.76, 30, and 60 % (from left to right); statistical metrics of fractional bias, fractional error, and R^2 for the comparison for both models are listed in Table S4 (fractional bias $= \frac{1}{N}\sum_{i=1}^{n}\frac{M-O}{\frac{M+O}{2}}$ and fractional error $= \frac{1}{N}\sum_{i=1}^{n}\frac{|M-O|}{\frac{M+O}{2}}$, where M is the predicted value, O is the observed value, and N is the sample size). The model–measurement comparison and the model skill was very poor when no IVOCs were included (fractional bias = −109 %, fractional error = 125 %, and $R^2 = 0.52$); this model reflects the treatment of diesel-powered sources in most traditional emissions inventories and large-scale models. The model–measurement comparison was reasonable with 13.76 % IVOCs (fractional bias = −46 %, fractional error = 101 %, and $R^2 = 0.95$) but model predictions were overpredicted with 60 % IVOCs (fractional bias = 72 %, fractional error = 97 %, and $R^2 = 0.99$). The optimal model performance that produced the lowest fractional bias and fractional error was realized at an IVOC mass fraction of 0.3 (fractional bias = 6 %, fractional error = 86 %, and $R^2 = 0.88$). For predictions with 30 % IVOCs, 66 % and 70 % of the model predictions were within a factor of 1.5 and 2 of the measurements and IVOCs on average accounted for 67 and 72 % (VBS and SOM, respectively) of the SOA at the highest photochemical exposure across all experiments. Given the optimal performance, the base case used in this work assumed 30 % IVOCs. These comparisons indicate that it is critical that IVOCs be included when modeling the SOA formation from diesel exhaust and also validate the IVOC composition estimates made by Zhao et al. (2015). We note that the model of Peng and Jimenez (2017) suggested that the organic compounds in the OFR experiments performed by Jathar et al. (2017a) may have been subjected to non-tropospheric photolysis at 185 and 254 nm. Accounting for the photolysis of the key SOA precursors (IVOCs and aromatics) could affect the optimal IVOC fraction identified above and hence needs to be considered in future work.

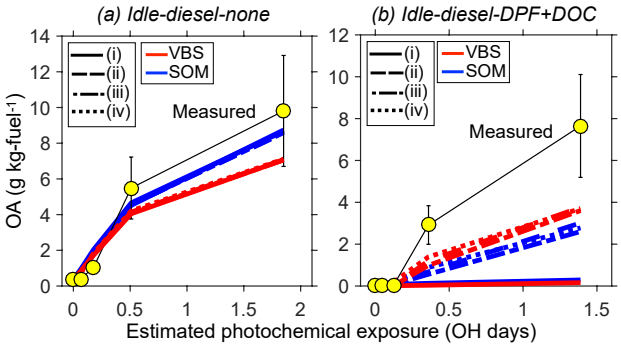

Figure 3. VBS and SOM model predictions of OA compared to measurements from the experiments performed on **(a)** 5 June (idle–diesel–none) and **(b)** 11 June (idle–diesel–DPF + DOC) as a function of photochemical age for four different particle size distribution inputs: (i) number mean diameter and measured number concentration at no OH exposure (solid), (ii) number mean diameter and measured number concentration at the given OH exposure (dash), (iii) average of (i) and (ii) (dash-dot), and (iv) nucleation of 1 nm particles (dot).

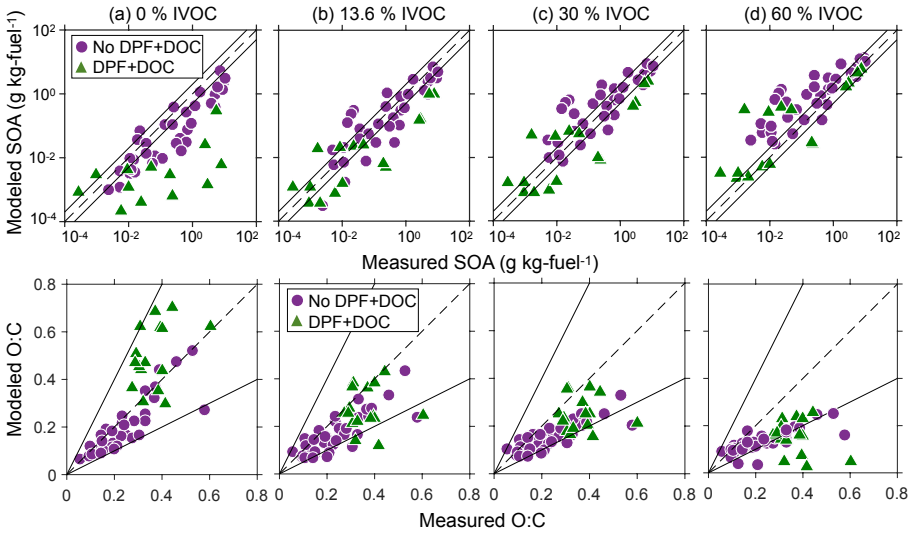

Figure 4. Scatter plot comparing SOM predictions of OA mass and O : C to measurements from all experiments at all photochemical ages at four different IVOC mass fractions: **(a)** 0 %, **(b)** 13.76 %, **(c)** 30 %, and **(d)** 60 %.

We further investigated the IVOC species that contributed the most to SOA formation. For 30 % IVOCs, cyclic alkane IVOCs accounted for 23 % of the THC emissions and on average accounted for 59 and 53 % (VBS and SOM, respectively) of the SOA formation across the different experiments. We should note that the speciation of cyclic alkane IVOCs in Zhao et al. (2015), while robust in quantifying the carbon number, did not include any specificity in terms of the molecular structure; i.e., their methods would not be able to distinguish between a pure C_{10} cyclic alkane and a cyclohexane with a 4-carbon branch. Further, the parameterizations to model SOA formation from cyclic alkane IVOCs for both models were based on the behavior of particular compounds. In the VBS model when using the high NO_x parameterizations, the surrogate for a cyclic alkane IVOC was determined through equivalence with a straight alkane IVOC, while in the VBS model when using the low NO_x parameterizations or the SOM the cyclic alkane IVOCs were tied to parameterizations for hexylcyclohexane. (The observed SOA yield and derived SOM parameterization for hexylcyclohexane are actually quite similar to that for cyclododecane for low NO_x conditions, but not for high NO_x conditions; Cappa et al., 2013.) This lack of specificity in the speciation and the SOA parameterizations made the SOA predictions from the oxidation of cyclic alkane IVOCs relatively uncertain. To examine the sensitivity of the model predictions to uncertainties in the model treatment of cyclic alkane IVOCs, we performed simulations with both models for one of the idle–diesel–none experiments where the cyclic alkane IVOCs were treated as branched alkane IVOCs; results from these simulations are shown in Fig. 5a. The use of branched alkane IVOCs to model cyclic alkane IVOCs only marginally reduced OA predictions for both the VBS and SOM models, suggesting that the model predictions were not sensitive to the SOA parameterization used for cyclic alkane IVOCs. Regardless, we recommend that future work focus on a more detailed speciation of cyclic alkane IVOCs in combustion emissions as well as on chamber and OFR experiments on those speciated compounds to improve quantification of their SOA mass yields.

As there were no direct measurements of any SOA precursors in the study of Jathar et al. (2017a), we have used previously published emissions profiles for diesel exhaust to determine initial concentrations of the SOA precursors. We examined the sensitivity of model predictions to two different emissions profiles from the EPA SPECIATE (version 4.3) database: Profile 3161 (included in the base case) and Profile 8774 (emissions from heavy duty diesel exhaust); the speciation for both profiles is provided in Tables S2 and S3. Both profiles only included speciation for VOC emissions and in these simulations we assumed an IVOC mass fraction of 0.3. The results captured in Fig. 5b for one of the idle–diesel–none experiments show that the choice in the emissions profile had no influence on the OA evolution for the VBS model but had a small influence on the OA evolution for the SOM. This relatively small influence was expected given that most of the SOA was formed from IVOC, rather than VOC, oxidation. This further demonstrates that IVOCs, not VOCs, play an important role in controlling the SOA formation from diesel exhaust emissions and it is important that future studies work towards better understanding the IVOC speciation.

The IVOC speciation of Zhao et al. (2015) included 37 unique species, each of which required a unique surrogate to model the SOA formation from that species. Tracking these many IVOC species in an atmospheric model (e.g., global climate model) may be intractable, and hence there is

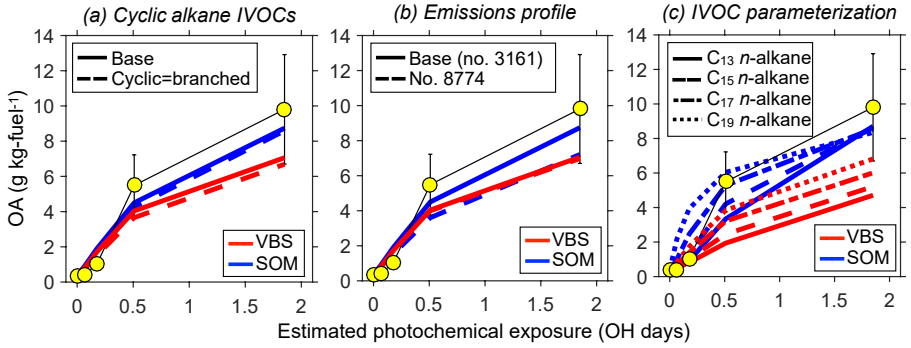

Figure 5. VBS and SOM predictions of OA compared to measurements from the experiment performed on 5 June (idle–diesel–none) as a function of photochemical age. Panel **(a)** examines uncertainty in model treatment of cyclic alkanes, panel **(b)** examines uncertainty in the VOC emissions profile, and panel **(c)** explores suitability of using a single surrogate linear alkane to model SOA formation from all IVOCs.

a need to develop simplified parameterizations to efficiently model SOA formation from IVOCs. We note that species using the same surrogate in the VBS model (e.g., a C_{15} linear alkane, C_{17} branched alkane, and C_{13} cyclic alkane are all parameterized using *n*-pentadecane when using the high NO_x parameterizations) could be lumped together to reduce the number of precursors and products tracked and that there are no penalties for a precursor type (e.g., *n*-alkanes) to include additional precursor and product species once a SOM grid is setup. Nonetheless, to investigate the possibility of developing a simplified parameterization, we modeled SOA from IVOCs assuming that all the IVOCs could be modeled together as a single linear C_{13}, C_{15}, C_{17}, or C_{19} alkane; a similar strategy was employed by Jathar et al. (2014b) to model SOA formation from unspeciated organic compounds in combustion emissions. Results from these simulations are shown in Fig. 5c for one of the idle–diesel–none experiments. For the VBS model, the use of a larger carbon number alkane to model IVOC SOA produced increasingly more OA, with the C_{19} alkane providing the best comparison against measurements. For the SOM, the use of a C_{13} and C_{15} alkane produced good agreement with measurements with a C_{13} alkane slightly underpredicting the OA at 0.5 OH days and the C_{15} alkane slightly overpredicting the OA at lower photochemical exposures (0.06 and 0.17 OH days). It was interesting to observe that for the SOM, in contrast to the VBS, the use of different linear alkanes produced different OA masses at lower photochemical exposures but converged at the highest photochemical exposure, suggesting that the effective SOA mass yield in the SOM varied dynamically with photochemical age. Differences in the VBS and SOM predictions with different alkane parameterizations point to inherent differences in the coupled representation of multigenerational aging and gas–particle partitioning. Results from these simulations indicate that in cases where computational efficiency is demanded, the SOA formation from IVOCs in diesel exhaust could be modeled using a surrogate linear alkane, possibly a C_{19} linear alkane with the VBS and a C_{13} or C_{15} linear alkane for the SOM.

3.4 Elemental composition

The SOM tracks both the carbon and oxygen number of the oxidation products, which allowed us to predict the O : C ratio of the OA. The O : C of the OA was calculated by combining the measured O : C of the POA with the modeled O : C of the SOA. We compare predictions of the O : C of OA from the SOM against measurements for all the experiments listed in Table 1 and at all photochemical exposures in Fig. 4; statistical metrics of fractional bias, fractional error, and R^2 for the comparison are listed in Table S5. Model predictions for the no IVOC case, where the O : C of the OA was dominated by the O : C of the aromatic SOA, compared well with measurements (fractional bias $= -4.2$ %, fractional error $= 28$ %, and $R^2 = 0.77$). However, the poor OA mass predictions with no IVOCs suggests that the good O : C performance was purely coincidental. The 13.76, 30, and 60 % IVOC cases underpredicted the OA O : C, where the underprediction appeared to increase as the IVOC influence increased (fractional bias $= -32$ %, fractional error $= 38$ %, and $R^2 = 0.72$ for the 13.76 % IVOC case; fractional bias $= -37$ %, fractional error $= 42$ %, and $R^2 = 0.70$ for the 30 % IVOC case; and fractional bias $= -60$ %, fractional error $= -62$ %, and $R^2 = 0.46$ for the 60 % IVOC case). A higher IVOC fraction resulted in a lower O : C ratio because the IVOCs were primarily composed of higher carbon number species that on oxidation produced low O : C SOA compared to SOA formed from precursors such as aromatics. On average, the 30 % IVOC case predicted an O : C ratio that was 28 % lower than the measurements. For the three non-zero IVOC cases (13.76, 30, and 60 %), the model skill in predicting the O : C was much better for the non-DPF + DOC experiments ($R^2 = 0.82$, 0.83, and 0.80, respectively) than for the DPF + DOC experiments ($R^2 = 0.02$, 0.02, and 0.29, respectively). Measurements and model predictions of the OA O : C

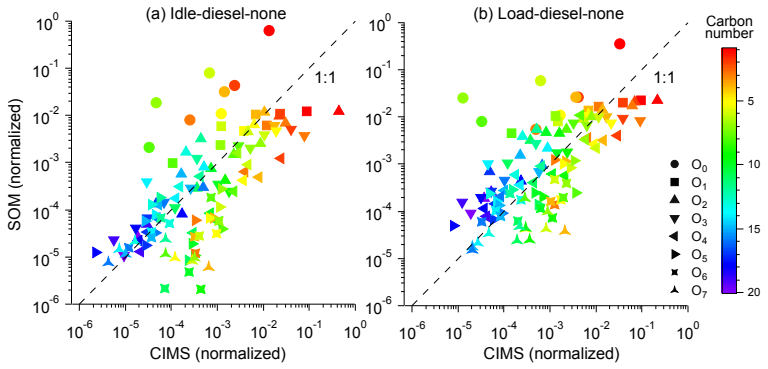

Figure 6. Normalized gas-phase concentration predictions from the SOM model for the idle–diesel–none and load–diesel–none experiments performed on 5 June and compared to normalized gas-phase concentrations measured by the CIMS.

ratio from the 30 % IVOC case as a function of photochemical age are presented in Fig. S2.

The underprediction in O : C ratios was confounding when compared to earlier applications of the SOM and in light of the reasonable model–measurement comparison found in this work in predicting OA mass. We note that the low O : C in the 13.76, 30, and 60 % IVOC cases stems from the dominance of product species that have high carbon numbers and low oxygen numbers. We explored several lines of reasoning for this underprediction. First, Cappa et al. (2013) found good agreement between the SOM-predicted and observed O : C for chamber experiments conducted using individual linear, branched and cyclic C_{12} alkanes. Also, general predictions of the dependence of O : C on the carbon number of the parent hydrocarbon (cf. Fig. 2b in Cappa and Wilson, 2012) show good agreement with observations (cf. Fig. 2a in Tkacik et al., 2012), in terms of both absolute values and shape. This suggests that uncertainties in the SOM parameters may not be the dominant reason for the underprediction. A possible reason for the underprediction then is that the compounds identified by Zhao et al. (2015) as IVOCs are structurally different than the alkanes used to model them in this work. Second, the gas-phase chemistry in the OFR might be inherently different than that in a chamber. For example, kinetic limitations to gas–particle partitioning may result in gas-phase oxidation of low-volatility products having high O : C that typically would have partitioned to the particle phase in a chamber experiment but instead are fragmented (Palm et al., 2016). Why the chamber-based SOM parameters then offer good model performance on OA mass remains unclear. One way in which this issue could be addressed in the future is by developing SOM parameters exclusively based on OFR data, as and when they become available. Third, the SOM used here did not include heterogeneous and particle-phase reactions that might influence the OA composition and O : C ratio. When heterogeneous reactions of OA were included assuming an OH uptake coefficient of 1 (the product distribution from the oxidation reaction was kept the same as the gas-phase reactions), SOA production at the highest photochemical exposure for all the experiments was reduced, on average, by 7 % from fragmentation reactions within the particle phase, but the O : C ratio was only marginally increased (average of 2 %).

To understand the O : C underprediction better, we compared model predictions of normalized gas-phase species concentrations from the SOM to normalized gas-phase measurements made by Friedman et al. (2017) using a CIMS. The CIMS detects an array of oxygenated organic species and the high resolution of the time-of-flight mass spectrometer enables identification of the elemental composition of each detected peak. The CIMS data were aggregated by carbon and oxygen number to facilitate comparison with the SOM data. The comparison was performed on a normalized basis because the CIMS did not provide absolute concentrations for every detected peak. The SOM–CIMS comparisons for the idle–diesel–none and load–diesel–none experiments at the highest photochemical exposure are shown in Fig. 6, which highlight four findings of note. First, the CIMS measured species larger than a carbon number of 12 that are presumably products from oxidation of higher molecular-weight organic compounds, although the possibility of dimer formation in the instrument cannot be entirely ruled out. Nonetheless, this provides additional evidence for the presence of IVOC oxidation products in diesel exhaust emissions. Second, the CIMS measured organic compounds with high O : C ratios (e.g., C_6O_6, C_7O_7). This implies that the reaction chemistry in OFRs rapidly adds functional groups to the carbon backbone, although larger, less oxidized compounds could be simultaneously functionalized and fragmented in the CIMS leading to the appearance of highly oxidized species. Third, the SOM offered a reasonable correlation against the CIMS measurements for both experiments across a majority of the carbon–oxygen combinations that spanned more than 4 orders of magnitude. Qualitatively, this finding validates the statistical evolution of organic compounds tracked through the generalized SOM mechanism, although certainly some differences are evident. Finally, for the mid-carbon number species ($\sim C_{10}$), the SOM seemed to

produce higher fractions of species with low oxygen numbers (O_0 to O_3) but lower fractions of species with high oxygen numbers (O_5 to O_7). This underprediction of the high oxygen number species might potentially explain why the SOM may be underpredicting the OA O : C ratio. The SOM–CIMS comparison is preliminary and we intend to explore the implications of this comparison in future work.

3.5 Other model sensitivities

We performed sensitivity analyses to examine the influence of other key processes on predictions from both the VBS and SOM models. When examining the sensitivity to each process, all the other inputs were kept the same as those listed in the base case. We only present sensitivity results for the idle–diesel–none experiment performed on 5 June, as the results for this experiment were generally representative of all experiments (Fig. 7). For completeness, we performed simulations for all the experiments at the highest photochemical exposure since each of the processes explored below manifested the strongest response at the highest photochemical exposure. The results from these simulations are presented as a change in the model predictions relative to that offered by the base case.

3.5.1 Multigenerational aging

One of the key differences between the VBS and the SOM models is how they represent the multigenerational aging of gas-phase products. SOA parameters for the VBS model represent stable product distributions at the end of the chamber experiments and therefore already include the influence of multigenerational aging reactions encountered during the chamber experiment. Additional multigenerational aging in the VBS model, based on the scheme of Robinson et al. (2007), is simulated as a continuous decrease in product volatility, which does not account for fragmentation reactions and has not been constrained against experiments. The SOM framework explicitly models multigenerational aging that includes treatment of fragmentation reactions and constrains the aging reactions based on the chamber experiments to an extent that is determined by the length (in OH exposure space) of the experiment. To test the influence of multigenerational aging, we performed model simulations with aging turned off for the VBS and SOM models and plot the results in Fig. 7a. We found that aging had a small influence ($\sim$ 18 % reduction in OA mass) on model predictions from the VBS model, most likely because the high SOA and OA mass concentrations resulted in a substantial fraction of the organic species to be partitioned to the particle phase. This left very little of the organic species in the gas phase to participate in multigenerational aging. We calculated that less than 20 % by mass of the product species in this experiment was in the gas phase at the OA mass concentration at the highest photochemical exposure, implying that the SOA mass yields

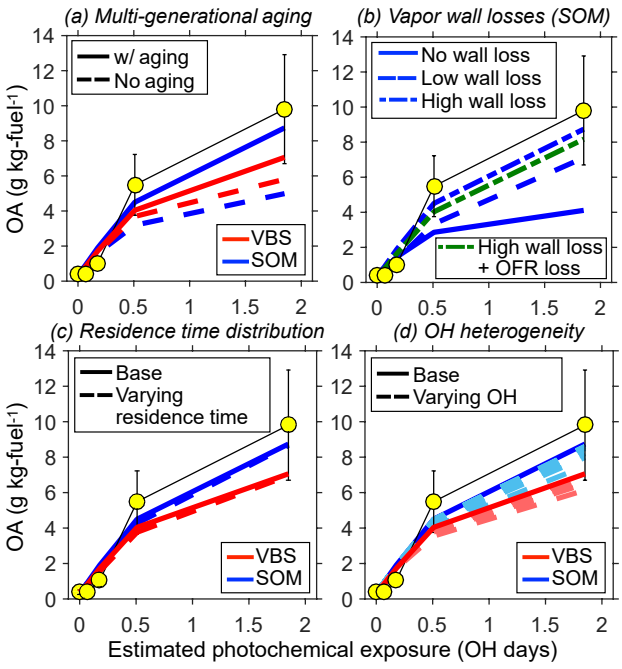

Figure 7. VBS and SOM predictions of OA compared to measurements from the experiment performed on 5 June (idle–diesel–none) as a function of photochemical age. Panels **(a)**–**(d)** examine the influence of multigenerational aging, vapor wall losses, residence time distribution, and spatial heterogeneity in OH concentrations, respectively. The dashed lines in panel **(d)** are deliberately lighter in color than the solid line to help differentiate the base result from the sensitivity results.

at these OA mass concentrations were rapidly approaching 100 %. In contrast, the absence of aging resulted in a 43 % decrease in the OA mass for the SOM. The decrease was mainly because the first-generation oxidation product with the highest yield (i.e., $C_x O_1$) was too volatile to partition to the particle phase and needed to be aged further to form condensable products. As noted earlier, the term aging is defined differently for the VBS and SOM models and the results presented here need to take the definitional issues into account when examining the influence of aging. Compared to the base case, no aging resulted in an average decrease of 6 and 30 % in OA mass for the VBS and SOM models, respectively, for all experiments at the highest photochemical exposure. These simulations suggest that aging of the oxidation products, at least for the SOM, is as important as the contribution of first-generation products to SOA formation.

3.5.2 Vapor wall losses

Prior work has highlighted the influence vapor wall losses exert on the calculation of SOA mass yields from chamber experiments (Zhang et al., 2014; Krechmer et al., 2016). Cappa et al. (2016), based on the chamber work of Zhang et al. (2014), recently published parameter sets for the SOM

that accounted for no vapor wall losses and two different vapor wall loss rates (1×10^{-4} and $2.5 \times 10^{-4}\,s^{-1}$) assuming an equivalent OA mass of the chamber walls of $10\,mg\,m^{-3}$ (the base case used the parameter sets for a vapor wall loss rate of $2.5 \times 10^{-4}\,s^{-1}$). We performed model simulations with SOM using parameters that were either not corrected for vapor wall losses or that were corrected for vapor wall losses using either the low (1×10^{-4}) or high (2.5×10^{-4}) estimates proposed by Cappa et al. (2016). The results plotted in Fig. 7b show that correcting for vapor wall losses significantly increased model-predicted OA mass (by 73 and 112 % for the low wall loss and high wall loss cases, respectively, at the highest photochemical exposure when compared to the case with no wall loss) and provided the best performance for the high estimate for vapor wall losses. Across all experiments and at the highest photochemical exposure, accounting for vapor wall losses using the high estimate resulted in an average increase of 39 % over not accounting for vapor wall losses. These comparisons suggest that it is important to use SOA parameterizations in which vapor wall losses in chambers have been accounted for when interpreting SOA experiments. Furthermore, we also simulated the influence of vapor losses to the OFR walls on model predictions. We assumed reversible uptake of vapors to the walls and used a vapor wall loss rate of $2.5 \times 10^{-3}\,s^{-1}$ (factor of ~ 10 larger than that for a chamber) based on the work of Palm et al. (2016) and an equivalent OA mass concentration of $10\,mg\,m^{-3}$ for the OFR walls. The results plotted in Fig. 7 show that the loss of vapors to the OFR walls had a small influence on model predictions: a 6.5 % decrease for this experiment and an average decrease of 11 % across all experiments at the highest photochemical exposure. Increasing the equivalent OA mass concentration for the OFR walls to 100 and $1000\,mg\,m^{-3}$ seemed to have no influence on model predictions. These findings imply that vapor wall losses in the presence of sufficient seed aerosol might not be of concern for OFRs (Lambe et al., 2015).

3.5.3 Residence time distributions

Model simulations performed in this work assumed that the OFR operated as a plug flow reactor with a constant residence time. Experimental studies by Lambe et al. (2011) and fluid dynamics simulations by Ortega et al. (2016) have shown that OFRs, particularly like the one used in this work, exhibit heterogeneity in residence times. We performed simulations to explore the sensitivity of varying residence times on model predictions. These simulations were performed based on a discretized version of the residence time distribution measured by Lambe et al. (2011) for SO_2 that yielded an average residence time of 100 s (same as that used by Jathar et al., 2017a). The discretized version included six parcels with volume fractions of 0.23, 0.36, 0.24, 0.11, 0.05, and 0.01 with residence times of 45, 65, 100, 200, 300, and 500 s, respectively. Each parcel experienced the same OH concentration but the varying residence times resulted in different OH exposures for each parcel. The parcels were combined after photochemical exposure without repartitioning the OA between the six parcels. Similar to the findings of Peng et al. (2015) for calculating OH exposure, our results in Fig. 7c show that using a residence time distribution had very little influence on the OA mass evolution compared to use of an effective average time. Compared to the base case, the residence time distribution resulted in an average decrease of 3 and 5 % in OA mass for the VBS and SOM models, respectively, for all experiments at the highest photochemical exposure.

3.5.4 Spatial heterogeneity in OH

In addition to the influence exerted by a distribution of residence times, spatial heterogeneity in the gas-phase chemistry inside the OFR (e.g., from radial variation in light intensity) could lead to spatial heterogeneity in OH concentrations and result in a distribution of OH exposures for the sample being aged. We performed simulations to explore the sensitivity of a varying OH exposure on model predictions. These simulations were performed where we split the sample coming into the OFR into two parcels and treated the parcels to different OH exposures. Each experiment was repeated for all combinations (ten total) of three different parcel splits (1/4–3/4, 1/3–2/3, 1/2–1/2) and two different OH exposure splits (1/3-X, 2/3-X); X was determined by conserving the total OH exposure reported by Jathar et al. (2017a). For instance, the first simulation was performed by splitting the OFR air parcel into 1/4 and 3/4 fractions by volume and exposing the 1/4 volume to 1/3 of the OH exposure. The parcels were combined after photochemical exposure without repartitioning the OA between the two parcels. The results in Fig. 7d show that the simulated spatial heterogeneity always reduced the OA mass although the maximum reduction (13 % for the VBS and 14 % for the SOM models) at the highest photochemical exposure was within the measurement uncertainty. Compared to the base case, the spatial heterogeneity in OH resulted in a maximum decrease of 14 and 15 % in OA mass for the VBS and SOM models, respectively, for all experiments at the highest photochemical exposure.

4 Summary and discussion

Recently, Jathar et al. (2017a) reported on experiments performed using the OFR to measure the photochemical production of SOA from diesel exhaust under varying engine loads, fuel types, and aftertreatment systems. These data present an opportunity to not only test SOA models but also use these models to interpret OFR data and determine their relevance for the real atmosphere. In this work, we applied two different SOA model frameworks (VBS and SOM) to simulate the photochemical production of SOA in an OFR from

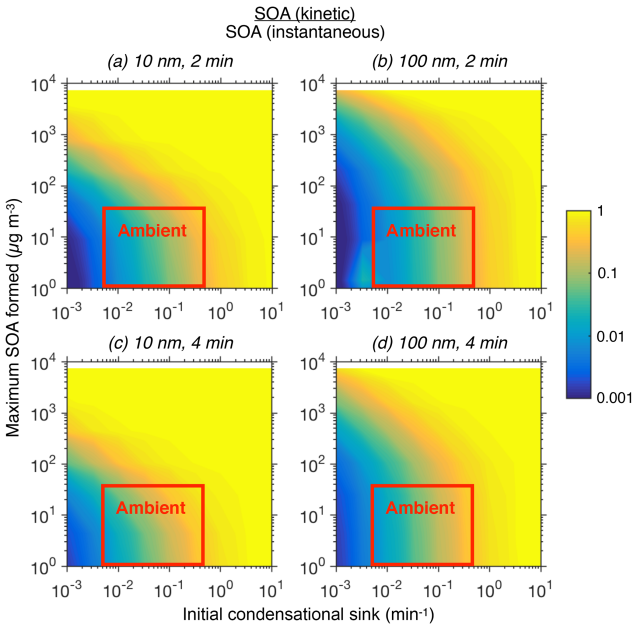

Figure 8. Model predictions of the ratio of SOA produced under kinetic partitioning assumptions to the SOA produced under instantaneous partitioning assumptions as a function of the initial condensational sink and the SOA formed under instantaneous partitioning. Panels are for calculations performed at two different particles sizes (10 and 100 nm) and two different residence times (2 and 4 min).

diesel exhaust and evaluated those model frameworks using the data from Jathar et al. (2017a). The VBS model is a parameterized model that allows for a volatility-based representation of OA while the SOM is a semi-explicit parameterized model that uses a carbon–oxygen grid to track OA. Both simulated the coupled chemistry, thermodynamic properties, and gas–particle partitioning of OA and accounted for (i) semi-volatile and reactive emissions of POA, (ii) SOA production from IVOCs and VOCs, (iii) NO_x-dependent parameterizations, (iv) multigenerational aging, and (v) kinetic gas–particle partitioning.

Model predictions suggest that the instantaneous gas–particle partitioning assumption may overpredict SOA formation in OFRs when the initial condensational sinks are low and the condensation of SOA is likely kinetically limited. Hence, SOA formation in OFRs needs to be modeled or interpreted through an explicit treatment of kinetic gas–particle partitioning. Differences in model predictions between instantaneous and kinetic partitioning will depend on the rate at which condensable SOA mass is produced in the OFR (depends on the initial precursor concentrations and composition and photochemical exposure), residence time in the OFR, properties of the condensing species (e.g., diffusion coefficient, molecular weight), and parameters relevant for partitioning (e.g., accommodation coefficient, seed aerosol surface area). To explore the relative importance of instantaneous and kinetically limited partitioning in an OFR, we used the SOM to simulate SOA formation from diluted diesel exhaust using instantaneous and kinetic partitioning assumptions for varying amounts of SOA formed (1–10 000 $\mu g\,m^{-3}$) and initial condensational sinks (0.001–10 min^{-1}). These simulations were similar to the calculations performed by Palm et al. (2017), where they calculated timescales and losses of condensable SOA vapors to the OFR walls and sampling lines and reaction with OH. The calculations were performed for two different initial particle sizes (10 and 100 nm) since the condensation of SOA mass would grow the initial condensational sink for the two particles at different rates; i.e., for the same starting initial condensational sink, smaller particles would experience quicker growth in the condensational sink compared to larger particles for the same amount of condensing mass. The calculations were also performed for two different residence times – 2 and 4 min – to span the residence time range used in typical applications of the OFR. We assumed a mass accommodation coefficient of 0.1. The results plotted in Fig. 8 show the ratio of SOA predicted through kinetic partitioning to that predicted through instantaneous partitioning as a function of the initial condensational sink and the SOA formed under an instantaneous partitioning assumption. Across the four scenarios explored (two initial particle sizes and two residence times), the SOA formation predicted under the kinetic partitioning assumption was an order of magnitude or more lower than that predicted under the instantaneous partitioning assumption over a large portion of the input range explored, e.g., when the initial condensational sink was smaller than $\sim 0.1\,min^{-1}$ and the maximum SOA formed was lower than $\sim 100\,\mu m^{-3}$ for the 10 nm simulations and lower than $\sim 1000\,\mu g\,m^{-3}$ for the 100 nm simulations. We also found that the SOA formation in the OFR was kinetically limited under typical ambient conditions. The SOA formation predicted under the kinetic partitioning assumption approached the SOA formed under the instantaneous partitioning assumption either when the initial condensational sink was very large ($> 5\,min^{-1}$) or when a large amount of condensable SOA was produced in the OFR ($>= 1000\,\mu g\,m^{-3}$ for the 10 nm particles and $> 10\,000\,\mu g\,m^{-3}$ for the 100 nm particles). Our finding implies that ambient applications of the OFR, where initial condensational sinks are typically smaller (~ 0.005–$0.5\,min^{-1}$) and the maximum SOA produced is typically less than $40\,\mu g\,m^{-3}$, will only produce a small fraction (0–30 %) of the intended SOA. Furthermore, our simulations suggested that a smaller initial particle size (i.e., 10 nm) for the same initial condensational sink and a longer OFR residence time (i.e., 4 min) may not necessarily help produce the intended SOA under ambient conditions. Although these simulation results need to be verified experimentally, they do suggest that it might be challenging to operate the OFR in conditions where instantaneous or atmospherically relevant partitioning is applicable, further complicating the coupled atmospheric simulation of chemistry and thermodynamics in OFRs.

Upon including IVOCs as SOA precursors, both the VBS and SOM models were able to reasonably predict the OA mass evolution reported by Jathar et al. (2017a) across different engine loads, fuel types, and aftertreatment systems. Model predictions suggest that 30 % of the unburned hydrocarbon emissions are likely IVOCs and that these IVOCs (regardless of the emissions profiles used to determine non-IVOC emissions) account for most (average of 70 %) of the SOA formed from diesel exhaust. These findings are consistent with prior work from chamber experiments (Jathar et al., 2014b) and modeling studies (Zhao et al., 2015). Simulations performed using single surrogates suggest that the complex mixture of IVOCs in diesel exhaust could be well represented using a linear C_{13} or C_{15} alkane for the SOM but might need a larger surrogate such as a C_{19} alkane for the VBS model. The need for a different surrogate species to model IVOC SOA between the SOM and VBS models most likely arises from differences in the coupled treatment of the oxidation chemistry and gas–particle partitioning in the OFR. The use of surrogates offers a computationally efficient strategy to model SOA formation from IVOCs in large-scale three-dimensional models. The SOM tracks the carbon and oxygen numbers of the oxidation products and hence model predictions were used to calculate atomic O : C ratios for OA, which were then compared to measurements. While the inclusion of IVOCs allowed for good model–measurement comparisons on OA mass, the SOM underpredicted the O : C ratio of OA on average by 28 %, possibly highlighting the limitations in modeling the IVOCs as alkanes and/or extrapolating chamber-based parameterizations to OFR experiments. Model predictions of the gas-phase organic species compared favorably to those measured using a CIMS, which qualitatively validates the statistical evolution of organic compounds tracked through the generalized SOM mechanism.

As OFRs are increasingly used to study SOA formation and evolution in laboratory and field environments, there is a need to develop models that can be used to interpret OFR data. This work suggests that multigenerational aging (in case of the VBS model), residence time distributions, and spatial heterogeneity in OH concentrations produced sensitivities that were well within the measurement uncertainty and were not a concern for the model system studied. However, model predictions did appear to be more sensitive to multigenerational aging (in case of the SOM) and influence of vapor wall losses, highlighting that these processes be included in OFR models. While the conclusions from this work may be relevant for other laboratory and ambient studies, their relative importance may vary. There are several instances where the model development was insufficient and will likely be addressed in future work. For example, the model could benefit from the use of a polydisperse size distribution to treat new particle formation and growth and improve predictions of the evolution of the aerosol size distribution. The model of Peng and Jimenez (2017) suggested that the SOA precursors and their oxidation products in the Jathar et al. (2017) experiments might have been subjected to non-tropospheric photolysis. Our work did not consider the photolysis of IVOCs (or other SOA precursors), which, if considered, may have implications for the IVOC findings reported here. We recommend that future studies on combustion sources significantly dilute their emissions before oxidizing them in an OFR while simultaneously accounting for photolysis reactions in models that simulate OFR chemistry. Finally, the model needs to be rigorously tested against other laboratory (e.g., Lambe et al., 2012) and ambient (e.g., Palm et al., 2016) OFR data.

Data availability. All measurements and select model predictions are archived at https://hdl.handle.net/10217/192200 (Eluri, 2018).

The Supplement related to this article is available online at https://doi.org/10.5194/acp-18-13813-2018-supplement.

Author contributions. SHJ and DKF designed the experiments. BF, DKF, and SHJ conducted experiments. SE, CDC, and SHJ conducted modeling. SE and SHJ wrote the paper, with contributions from all co-authors.

Competing interests. The authors declare that they have no conflict of interest.

Acknowledgements. We thank Zhe Peng and Jose Jimenez for running their oxidation flow reactor model (Peng and Jimenez, 2017) to provide NO_x relevant inputs for our work. We thank the Jeffrey Pierce and John Volckens for their feedback on the written manuscript. Delphine K. Farmer acknowledges the Beckman Young Investigator Award for funding.

Edited by: Barbara Ervens
Reviewed by: three anonymous referees

References

Ahlberg, E., Falk, J., Eriksson, A., Holst, T., Brune, W. H., Kristensson, A., Roldin, P., and Svenningsson, B.: Secondary organic aerosol from VOC mixtures in an oxidation flow reactor, Atmos. Environ., 161, 210–220, 2017.

Ahmadov, R., McKeen, S. A., Robinson, A. L., Bahreini, R., Middlebrook, A. M., de Gouw, J. A., Meagher, J., Hsie, E. Y., Edgerton, E., Shaw, S., and Trainer, M.: A volatility basis set model for summertime secondary organic aerosols over the eastern United States in 2006, J. Geophys. Res.-Atmos., 117, D06301, https://doi.org/10.1029/2011JD016831, 2012.

Anderson, J. O., Thundiyil, J. G., and Stolbach, A.: Clearing the air: a review of the effects of particulate matter air pollution on human health, J. Med. Toxicol., 8, 166–175, 2012.

Atkinson, R. and Arey, J.: Atmospheric degradation of volatile organic compounds, Chem. Rev., 103, 4605–4638, 2003.

Bond, T., Venkataraman, C., and Masera, O.: Global atmospheric impacts of residential fuels, Energy Sustain. Dev., 8, 20–32, 2004.

Cappa, C. D. and Wilson, K. R.: Multi-generation gas-phase oxidation, equilibrium partitioning, and the formation and evolution of secondary organic aerosol, Atmos. Chem. Phys., 12, 9505–9528, https://doi.org/10.5194/acp-12-9505-2012, 2012.

Cappa, C. D., Zhang, X., Loza, C. L., Craven, J. S., Yee, L. D., and Seinfeld, J. H.: Application of the Statistical Oxidation Model (SOM) to Secondary Organic Aerosol formation from photooxidation of C_{12} alkanes, Atmos. Chem. Phys., 13, 1591–1606, https://doi.org/10.5194/acp-13-1591-2013, 2013.

Cappa, C. D., Jathar, S. H., Kleeman, M. J., Docherty, K. S., Jimenez, J. L., Seinfeld, J. H., and Wexler, A. S.: Simulating secondary organic aerosol in a regional air quality model using the statistical oxidation model – Part 2: Assessing the influence of vapor wall losses, Atmos. Chem. Phys., 16, 3041–3059, https://doi.org/10.5194/acp-16-3041-2016, 2016.

Chacon-Madrid, H. and Donahue, N.: Fragmentation vs. functionalization: chemical aging and organic aerosol formation, Atmos. Chem. Phys, 11, 10553–10563, https://doi.org/10.5194/acp-11-10553-2011, 2011.

Chan, A. W. H., Kautzman, K. E., Chhabra, P. S., Surratt, J. D., Chan, M. N., Crounse, J. D., Kürten, A., Wennberg, P. O., Flagan, R. C., and Seinfeld, J. H.: Secondary organic aerosol formation from photooxidation of naphthalene and alkylnaphthalenes: implications for oxidation of intermediate volatility organic compounds (IVOCs), Atmos. Chem. Phys., 9, 3049–3060, https://doi.org/10.5194/acp-9-3049-2009, 2009.

Chen, S., Brune, W. H., Lambe, A. T., Davidovits, P., and Onasch, T. B.: Modeling organic aerosol from the oxidation of α-pinene in a Potential Aerosol Mass (PAM) chamber, Atmos. Chem. Phys., 13, 5017–5031, https://doi.org/10.5194/acp-13-5017-2013, 2013.

Chirico, R., DeCarlo, P. F., Heringa, M. F., Tritscher, T., Richter, R., Préôt, A. S. H., Dommen, J., Weingartner, E., Wehrle, G., Gysel, M., Laborde, M., and Baltensperger, U.: Impact of aftertreatment devices on primary emissions and secondary organic aerosol formation potential from in-use diesel vehicles: results from smog chamber experiments, Atmos. Chem. Phys., 10, 11545–11563, https://doi.org/10.5194/acp-10-11545-2010, 2010.

Donahue, N. M., Robinson, A., Stanier, C., and Pandis, S.: Coupled partitioning, dilution, and chemical aging of semivolatile organics, Environ. Sci. Technol., 40, 2635–2643, https://doi.org/10.1021/es052297c, 2006a.

Donahue, N. M., Robinson, A. L., Stanier, C. O., and Pandis, S. N.: Coupled partitioning, dilution, and chemical aging of semivolatile organics, Environ. Sci. Technol., 40, 2635–2643, 2006b.

Donahue, N. M., Epstein, S. A., Pandis, S. N., and Robinson, A. L.: A two-dimensional volatility basis set: 1. organic-aerosol mixing thermodynamics, Atmos. Chem. Phys., 11, 3303–3318, https://doi.org/10.5194/acp-11-3303-2011, 2011.

Dzepina, K., Volkamer, R., Madronich, S., Tulet, P., Ulbrich, I., Zhang, Q., Cappa, C., Ziemann, P., and Jimenez, J.: Evaluation of recently-proposed secondary organic aerosol models for a case study in Mexico City, Atmos. Chem. Phys., 9, 5681–5709, https://doi.org/10.5194/acp-9-5681-2009, 2009.

Eluri, S., Cappa, C. D., Friedman, B., Farmer, D. K., and Jathar, S.: Supporting data for the manuscript: Modeling the formation and composition of secondary organic aerosol from diesel exhaust using parameterized and semi-explicit chemistry and thermodynamic models, available at: https://hdl.handle.net/10217/192200, last access: September 2018.

Ensberg, J. J., Hayes, P. L., Jimenez, J. L., Gilman, J. B., Kuster, W. C., de Gouw, J. A., Holloway, J. S., Gordon, T. D., Jathar, S., Robinson, A. L., and Seinfeld, J. H.: Emission factor ratios, SOA mass yields, and the impact of vehicular emissions on SOA formation, Atmos. Chem. Phys., 14, 2383–2397, https://doi.org/10.5194/acp-14-2383-2014, 2014.

EPA: SPECIATE Version 4.3, US EPA, available at: ttps://www.epa.gov/sites/production/files/2015-10/speciate43_20110928.zip (last access: 30 July 2018), 2011.

EPA: Estimation Programs Interface Suite^{TM}, United States Environmental Protection Agency, Washington, D.C., USA, 2017.

Friedman, B., Brophy, P., Brune, W. H., and Farmer, D. K.: Anthropogenic Sulfur Perturbations on Biogenic Oxidation: SO2 Additions Impact Gas-Phase OH Oxidation Products of α- and β-Pinene, Environ. Sci. Technol., 50, 1269–1279, https://doi.org/10.1021/acs.est.5b05010, 2016.

Friedman, B., Link, M. F., Fulgham, S. R., Brophy, P., Galang, A., Brune, W. H., Jathar, S. H., and Farmer, D. K.: Primary and Secondary Sources of Gas-Phase Organic Acids from Diesel Exhaust, Environ. Sci. Technol., 51, 10872–10880, https://doi.org/10.1021/acs.est.7b01169, 2017.

Fuzzi, S., Baltensperger, U., Carslaw, K., Decesari, S., Denier van der Gon, H., Facchini, M. C., Fowler, D., Koren, I., Langford, B., Lohmann, U., Nemitz, E., Pandis, S., Riipinen, I., Rudich, Y., Schaap, M., Slowik, J. G., Spracklen, D. V., Vignati, E., Wild, M., Williams, M., and Gilardoni, S.: Particulate matter, air quality and climate: lessons learned and future needs, Atmos. Chem. Phys., 15, 8217–8299, https://doi.org/10.5194/acp-15-8217-2015, 2015.

Gentner, D. R., Jathar, S. H., Gordon, T. D., Bahreini, R., Day, D. A., El Haddad, I., Hayes, P. L., Pieber, S. M., Platt, S. M., and de Gouw, J. A.: A review of urban secondary organic aerosol formation from gasoline and diesel motor vehicle emissions, Environ. Sci. Technol., 51, 1074–1093, https://doi.org/10.1021/acs.est.6b04509, 2017.

Gordon, T. D., Nguyen, N. T., Presto, A. A., Lipsky, E. M., Maldonado, S., Maricq, M., and Robinson, A. L.: Secondary organic aerosol production from diesel vehicle exhaust: impact of aftertreatment, fuel chemistry and driving cycle, Atmos. Chem. Phys., 14, 4643–4659, https://doi.org/10.5194/acp-14-4643-2014, 2014.

Hayes, P. L., Carlton, A. G., Baker, K. R., Ahmadov, R., Washenfelder, R. A., Alvarez, S., Rappenglück, B., Gilman, J. B., Kuster, W. C., de Gouw, J. A., Zotter, P., Prévôt, A. S. H., Szidat, S., Kleindienst, T. E., Offenberg, J. H., Ma, P. K., and Jimenez, J. L.: Modeling the formation and aging of secondary organic aerosols in Los Angeles during CalNex 2010, Atmos. Chem. Phys., 15, 5773–5801, https://doi.org/10.5194/acp-15-5773-2015, 2015.

Hildebrandt, L., Donahue, N., and Pandis, S.: High formation of secondary organic aerosol from the photo-oxidation of toluene,

Atmos. Chem. Phys., 9, 2973–2986, https://doi.org/10.5194/acp-9-2973-2009, 2009.

Hodzic, A., Jimenez, J., Madronich, S., Canagaratna, M., DeCarlo, P., Kleinman, L., and Fast, J.: Modeling organic aerosols in a megacity: potential contribution of semi-volatile and intermediate volatility primary organic compounds to secondary organic aerosol formation, Atmos. Chem. Phys., 10, 5491–5514, https://doi.org/10.5194/acp-10-5491-2010, 2010.

Huffman, J., Docherty, K., Mohr, C., Cubison, M., Ulbrich, I., Ziemann, P., Onasch, T., and Jimenez, J.: Chemically-resolved volatility measurements of organic aerosol from different sources, Environ. Sci. Technol., 43, 5351–5357, 2009.

Jathar, S. H., Farina, S., Robinson, A., and Adams, P.: The influence of semi-volatile and reactive primary emissions on the abundance and properties of global organic aerosol, Atmos. Chem. Phys., 11, 7727–7746, https://doi.org/10.5194/acp-11-7727-2011, 2011.

Jathar, S. H., Donahue, N. M., Adams, P. J., and Robinson, A. L.: Testing secondary organic aerosol models using smog chamber data for complex precursor mixtures: influence of precursor volatility and molecular structure, Atmos. Chem. Phys., 14, 5771–5780, https://doi.org/10.5194/acp-14-5771-2014, 2014a.

Jathar, S. H., Gordon, T. D., Hennigan, C. J., Pye, H. O. T., Pouliot, G. A., Adams, P. J., Donahue, N. M., and Robinson, A. L.: Unspeciated organic emissions from combustion sources and their influence on the secondary organic aerosol budget in the United States, P. Natl. Acad. Sci. USA, 111, 10473–10478, 2014b.

Jathar, S. H., Cappa, C. D., Wexler, A. S., Seinfeld, J. H., and Kleeman, M. J.: Multi-generational oxidation model to simulate secondary organic aerosol in a 3-D air quality model, Geosci. Model Dev., 8, 2553–2567, https://doi.org/10.5194/gmd-8-2553-2015, 2015.

Jathar, S. H., Cappa, C. D., Wexler, A. S., Seinfeld, J. H., and Kleeman, M. J.: Simulating secondary organic aerosol in a regional air quality model using the statistical oxidation model – Part 1: Assessing the influence of constrained multi-generational ageing, Atmos. Chem. Phys., 16, 2309–2322, https://doi.org/10.5194/acp-16-2309-2016, 2016.

Jathar, S. H., Friedman, B., Galang, A. A., Link, M. F., Brophy, P., Volckens, J., Eluri, S., and Farmer, D. K.: Linking Load, Fuel and Emission Controls to Photochemical Production of Secondary Organic Aerosol from a Diesel Engine, Environ. Sci. Technol., 51, 1377–1386, https://doi.org/10.1021/acs.est.6b04602, 2017a.

Jathar, S. H., Woody, M., Pye, H. O. T., Baker, K. R., and Robinson, A. L.: Chemical transport model simulations of organic aerosol in southern California: model evaluation and gasoline and diesel source contributions, Atmos. Chem. Phys., 17, 4305–4318, https://doi.org/10.5194/acp-17-4305-2017, 2017b.

Karnezi, E., Riipinen, I., and Pandis, S. N.: Measuring the atmospheric organic aerosol volatility distribution: a theoretical analysis, Atmos. Meas. Tech., 7, 2953–2965, https://doi.org/10.5194/amt-7-2953-2014, 2014.

Konovalov, I. B., Beekmann, M., Berezin, E. V., Petetin, H., Mielonen, T., Kuznetsova, I. N., and Andreae, M. O.: The role of semi-volatile organic compounds in the mesoscale evolution of biomass burning aerosol: a modeling case study of the 2010 mega-fire event in Russia, Atmos. Chem. Phys., 15, 13269–13297, https://doi.org/10.5194/acp-15-13269-2015, 2015.

Krechmer, J. E., Pagonis, D., Ziemann, P. J., and Jimenez, J. L. L.: Quantification of gas-wall partitioning in Teflon environmental chambers using rapid bursts of low-volatility oxidized species generated in-situ, Environ. Sci. Technol., 50, 5757–5765, https://doi.org/10.1021/acs.est.6b00606, 2016.

Krechmer, J. E., Day, D. A., Ziemann, P. J., and Jimenez, J. L.: Direct measurements of gas/particle partitioning and mass accommodation coefficients in environmental chambers, Environ. Sci. Technol., 51, 11867–11875, 2017.

Kroll, J. H., Smith, J. D., Che, D. L., Kessler, S. H., Worsnop, D. R., and Wilson, K. R.: Measurement of fragmentation and functionalization pathways in the heterogeneous oxidation of oxidized organic aerosol, Phys. Chem. Chem. Phys., 11, 8005–8014, 2009.

Lambe, A. T., Ahern, A. T., Williams, L. R., Slowik, J. G., Wong, J. P. S., Abbatt, J. P. D., Brune, W. H., Ng, N. L., Wright, J. P., Croasdale, D. R., Worsnop, D. R., Davidovits, P., and Onasch, T. B.: Characterization of aerosol photooxidation flow reactors: heterogeneous oxidation, secondary organic aerosol formation and cloud condensation nuclei activity measurements, Atmos. Meas. Tech., 4, 445–461, https://doi.org/10.5194/amt-4-445-2011, 2011.

Lambe, A. T., Onasch, T. B., Croasdale, D. R., Wright, J. P., Martin, A. T., Franklin, J. P., Massoli, P., Kroll, J. H., Canagaratna, M. R., and Brune, W. H.: Transitions from functionalization to fragmentation reactions of laboratory secondary organic aerosol (SOA) generated from the OH oxidation of alkane precursors, Environ. Sci. Technol., 46, 5430–5437, 2012.

Lambe, A. T., Chhabra, P. S., Onasch, T. B., Brune, W. H., Hunter, J. F., Kroll, J. H., Cummings, M. J., Brogan, J. F., Parmar, Y., Worsnop, D. R., Kolb, C. E., and Davidovits, P.: Effect of oxidant concentration, exposure time, and seed particles on secondary organic aerosol chemical composition and yield, Atmos. Chem. Phys., 15, 3063–3075, https://doi.org/10.5194/acp-15-3063-2015, 2015.

Lee, B.-H., Pierce, J. R., Engelhart, G. J., and Pandis, S. N.: Volatility of secondary organic aerosol from the ozonolysis of monoterpenes, Atmos. Environ., 45, 2443–2452, 2011.

Lim, Y. B. and Ziemann, P. J.: Effects of molecular structure on aerosol yields from OH radical-initiated reactions of linear, branched, and cyclic alkanes in the presence of NO_x, Environ. Sci. Technol., 43, 2328–2334, 2009.

Link, M., Friedman, B., Fulgham, R., Brophy, P., Galang, A., Jathar, S., Veres, P., Roberts, J., and Farmer, D.: Photochemical processing of diesel fuel emissions as a large secondary source of isocyanic acid (HNCO), Geophys. Res. Lett., 43, 4033–4041, 2016.

Loza, C. L., Craven, J. S., Yee, L. D., Coggon, M. M., Schwantes, R. H., Shiraiwa, M., Zhang, X., Schilling, K. A., Ng, N. L., Canagaratna, M. R., Ziemann, P. J., Flagan, R. C., and Seinfeld, J. H.: Secondary organic aerosol yields of 12-carbon alkanes, Atmos. Chem. Phys., 14, 1423–1439, https://doi.org/10.5194/acp-14-1423-2014, 2014.

May, A. A., Levin, E. J. T., Hennigan, C. J., Riipinen, I., Lee, T., Collett, J. L., Jimenez, J. L., Kreidenweis, S. M., and Robinson, A. L.: Gas-particle partitioning of primary organic aerosol emissions: 3. Biomass burning, J. Geophys. Res.-Atmos., 118, 11327–11338, https://doi.org/10.1002/jgrd.50828, 2013a.

May, A. A., Presto, A. A., Hennigan, C. J., Nguyen, N. T., Gordon, T. D., and Robinson, A. L.: Gas-particle partitioning of

primary organic aerosol emissions: (2) Diesel vehicles, Environ. Sci. Technol., 47, 8288–8296, 2013b.

May, A. A., Presto, A. A., Hennigan, C. J., Nguyen, N. T., Gordon, T. D., and Robinson, A. L.: Gas-particle partitioning of primary organic aerosol emissions: (1) gasoline vehicle exhaust, Atmos. Environ., 77, 128–139, 2013c.

Murphy, B. and Pandis, S.: Simulating the formation of semivolatile primary and secondary organic aerosol in a regional chemical transport model, Environ. Sci. Technol., 43, 4722–4728, https://doi.org/10.1021/es803168a, 2009.

Ng, N., Kroll, J., Chan, A., Chhabra, P., Flagan, R., and Seinfeld, J.: Secondary organic aerosol formation from m-xylene, toluene, and benzene, Atmos. Chem. Phys., 7, 3909–3922, https://doi.org/10.5194/acp-7-3909-2007, 2007.

Odum, J. R., Hoffmann, T., Bowman, F., Collins, D., Flagan, R. C., and Seinfeld, J. H.: Gas/particle partitioning and secondary organic aerosol yields, Environ. Sci. Technol., 30, 2580–2585, 1996.

Ortega, A. M., Hayes, P. L., Peng, Z., Palm, B. B., Hu, W., Day, D. A., Li, R., Cubison, M. J., Brune, W. H., Graus, M., Warneke, C., Gilman, J. B., Kuster, W. C., de Gouw, J., Gutiérrez-Montes, C., and Jimenez, J. L.: Real-time measurements of secondary organic aerosol formation and aging from ambient air in an oxidation flow reactor in the Los Angeles area, Atmos. Chem. Phys., 16, 7411–7433, https://doi.org/10.5194/acp-16-7411-2016, 2016.

Pachauri, R. K., Allen, M. R., Barros, V. R., Broome, J., Cramer, W., Christ, R., Church, J. A., Clarke, L., Dahe, Q., Dasgupta, P., Dubash, N. K., Edenhofer, O., Elgizouli, I., Field, C. B., Forster, P., Friedlingstein, P., Fuglestvedt, J., Gomez-Echeverri, L., Hallegatte, S., Hegerl, G., Howden, M., Jiang, K., Jimenez Cisneroz, B., Kattsov, V., Lee, H., Mach, K. J., Marotzke, J., Mastrandrea, M. D., Meyer, L., Minx, J., Mulugetta, Y., O'Brien, K., Oppenheimer, M., Pereira, J. J., Pichs-Madruga, R., Plattner, G. K., Pörtner, H.-O., Power, S. B., Preston, B., Ravindranath, N. H., Reisinger, A., Riahi, K., Rusticucci, M., Scholes, R., Seyboth, K., Sokona, Y., Stavins, R., Stocker, T. F., Tschakert, P., van Vuuren, D., and van Ypserle, J. P.: Climate Change 2014: Synthesis Report, in: Contribution of Working Groups I, II and III to the Fifth Assessment Report of the Intergovernmental Panel on Climate Change, edited by: Pachauri, R. K. and Meyer, L., IPCC, Geneva, Switzerland, 151 pp., 2014.

Palm, B. B., Campuzano-Jost, P., Ortega, A. M., Day, D. A., Kaser, L., Jud, W., Karl, T., Hansel, A., Hunter, J. F., Cross, E. S., Kroll, J. H., Peng, Z., Brune, W. H., and Jimenez, J. L.: In situ secondary organic aerosol formation from ambient pine forest air using an oxidation flow reactor, Atmos. Chem. Phys., 16, 2943–2970, https://doi.org/10.5194/acp-16-2943-2016, 2016.

Palm, B. B., Campuzano-Jost, P., Day, D. A., Ortega, A. M., Fry, J. L., Brown, S. S., Zarzana, K. J., Dube, W., Wagner, N. L., Draper, D. C., Kaser, L., Jud, W., Karl, T., Hansel, A., Gutiérrez-Montes, C., and Jimenez, J. L.: Secondary organic aerosol formation from in situ OH, O_3, and NO_3 oxidation of ambient forest air in an oxidation flow reactor, Atmos. Chem. Phys., 17, 5331–5354, https://doi.org/10.5194/acp-17-5331-2017, 2017.

Pankow, J. F.: An absorption model of gas/particle partitioning of organic compounds in the atmosphere, Atmos. Environ., 28, 185–188, 1994.

Pankow, J. F. and Barsanti, K. C.: The carbon number-polarity grid: A means to manage the complexity of the mix of organic compounds when modeling atmospheric organic particulate matter, Atmos. Environ., 43, 2829–2835, 2009.

Peng, Z. and Jimenez, J. L.: Modeling of the chemistry in oxidation flow reactors with high initial NO, Atmos. Chem. Phys., 17, 11991–12010, https://doi.org/10.5194/acp-17-11991-2017, 2017.

Peng, Z., Day, D. A., Stark, H., Li, R., Lee-Taylor, J., Palm, B. B., Brune, W. H., and Jimenez, J. L.: HO_x radical chemistry in oxidation flow reactors with low-pressure mercury lamps systematically examined by modeling, Atmos. Meas. Tech., 8, 4863–4890, https://doi.org/10.5194/amt-8-4863-2015, 2015.

Presto, A. A., Miracolo, M. A., Donahue, N. M., and Robinson, A. L.: Secondary organic aerosol formation from high-NO_x photooxidation of low volatility precursors: n-alkanes, Environ. Sci. Technol., 44, 2029–2034, 2010.

Presto, A. A., Nguyen, N. T., Ranjan, M., Reeder, A. J., Lipsky, E. M., Hennigan, C. J., Miracolo, M. A., Riemer, D. D., and Robinson, A. L.: Fine particle and organic vapor emissions from staged tests of an in-use aircraft engine, Atmos. Environ., 45, 3603–3612, 2011.

Pye, H. and Seinfeld, J.: A global perspective on aerosol from low-volatility organic compounds, Atmos. Chem. Phys, 10, 4377–4401, https://doi.org/10.5194/acp-10-4377-2010, 2010.

Robinson, A. L., Donahue, N. M., Shrivastava, M. K., Weitkamp, E. A., Sage, A. M., Grieshop, A. P., Lane, T. E., Pierce, J. R., and Pandis, S. N.: Rethinking organic aerosols: Semivolatile emissions and photochemical aging, Science, 315, 1259–1262, 2007.

Saleh, R., Donahue, N. M., and Robinson, A. L.: Time scales for gas-particle partitioning equilibration of secondary organic aerosol formed from alpha-pinene ozonolysis, Environ. Sci. Technol., 47, 5588–5594, 2013.

Seinfeld, J. H. and Pandis, S. N.: Atmospheric Chemistry and Physics, John Wiley and Sons, New York, 2006.

Simonen, P., Saukko, E., Karjalainen, P., Timonen, H., Bloss, M., Aakko-Saksa, P., Rönkkö, T., Keskinen, J., and Dal Maso, M.: A new oxidation flow reactor for measuring secondary aerosol formation of rapidly changing emission sources, Atmos. Meas. Tech., 10, 1519–1537, https://doi.org/10.5194/amt-10-1519-2017, 2017.

Song, C., Na, K., Warren, B., Malloy, Q., and Cocker III, D. R.: Secondary organic aerosol formation from the photooxidation of p-and o-xylene, Environ. Sci. Technol., 41, 7403–7408, 2007.

Tang, M. J., Shiraiwa, M., Pöschl, U., Cox, R. A., and Kalberer, M.: Compilation and evaluation of gas phase diffusion coefficients of reactive trace gases in the atmosphere: Volume 2. Diffusivities of organic compounds, pressure-normalised mean free paths, and average Knudsen numbers for gas uptake calculations, Atmos. Chem. Phys., 15, 5585–5598, https://doi.org/10.5194/acp-15-5585-2015, 2015.

Tkacik, D. S., Presto, A. A., Donahue, N. M., and Robinson, A. L.: Secondary organic aerosol formation from intermediate-volatility organic compounds: cyclic, linear, and branched alkanes, Environ. Sci. Technol., 46, 8773–8781, https://doi.org/10.1021/es301112c, 2012.

Tkacik, D. S., Lambe, A. T., Jathar, S., Li, X., Presto, A. A., Zhao, Y., Blake, D., Meinardi, S., Jayne, J. T., Croteau, P. L., and Robinson, A. L.: Secondary Organic Aerosol Forma-

tion from in-Use Motor Vehicle Emissions Using a Potential Aerosol Mass Reactor, Environ. Sci. Technol., 48, 11235–11242, https://doi.org/10.1021/es502239v, 2014.

Tsimpidi, A., Karydis, V., Zavala, M., Lei, W., Molina, L., Ulbrich, I., Jimenez, J., and Pandis, S.: Evaluation of the volatility basis-set approach for the simulation of organic aerosol formation in the Mexico City metropolitan area, Atmos. Chem. Phys, 10, 525–546, https://doi.org/10.5194/acp-10-525-2010, 2009.

Zhang, X., Cappa, C. D., Jathar, S. H., McVay, R. C., Ensberg, J. J., Kleeman, M. J., and Seinfeld, J. H.: Influence of vapor wall loss in laboratory chambers on yields of secondary organic aerosol, P. Natl. Acad. Sci. USA, 111, 5802–5807, 2014.

Zhao, Y., Nguyen, N. T., Presto, A. A., Hennigan, C. J., May, A. A., and Robinson, A. L.: Intermediate volatility organic compound emissions from on-road diesel vehicles: chemical composition, emission factors, and estimated secondary organic aerosol production, Environ. Sci. Technol., 49, 11516–11526, 2015.